Layer-Number Dependent Optical Properties of 2D Materials and Their Application for Thickness Determination

*Xiao-Li Li, Wen-Peng Han, Jiang-Bin Wu, Xiao-Fen Qiao, Jun Zhang, and Ping-Heng Tan**

The quantum confinement in atomic scale and the presence of interlayer coupling in multilayer make the electronic and optical properties of 2D materials (2DMs) be dependent on the layer number (*N*) from monolayer to multilayer. Optical properties of 2DMs have been widely probed by several optical techniques, such as optical contrast, Rayleigh scattering, Raman spectroscopy, optical absorption, photoluminescence, and second harmonic generation. Here, it is reviewed how optical properties of several typical 2DMs (e.g., monolayer and multilayer graphenes, transition metal dichalcogenides) probed by these optical techniques significantly depend on *N*. Further, it has been demonstrated how these optical techniques service as fast and nondestructive approaches for *N* counting or thickness determination of these typical 2DM flakes. The corresponding approaches can be extended to the whole 2DM family produced by micromechanical exfoliations, chemical-vapor-deposition growth, or transfer processes on various substrates, which bridges the gap between the characterization and international standardization for thickness determination of 2DM flakes.

1. Introduction

2D materials (2DMs) can be usually exfoliated from layered materials (LMs), which form strong chemical bonds in-plane but display weak van der Waals (vdW) bonding out-of-plane.[1–3] Up to now, 2DMs are explored to constitute a large family including the graphene-like family, 2D dichalcogenides and 2D oxides, of which physical properties range from insulators (BN,[4] HfS_2,[5] etc.), topological insulators (Bi_2Se_3,[6,7] Bi_2Te_3,[6] etc.), semiconductors (MX_2, M = Mo, W; X = S, Se),[8–10] GaSe, GaS,[11] CuS, $SnSe_2$, $PbSnS_2$, GeSe, InSe,[12] SnS, $ReSe_2$, etc.), semi-metals (graphene,[13] WTe_2[14,15]) to superconductors[3,16] ($NbSe_2$, NbS_2, FeSe, FeTe, etc.). The symmetries of 2DM crystals include D_{6h} (graphite, MX_2, GaSe(S), CuS, $SnS(Se)_2$, $TaS(Se)_2$, FeTe(Se), $NbSe_2$, and h-BN), D_{3d} ($SnSe_2$ and $Bi_2Te(Se)_3$), D_{2h} (black phosphorus (BP),[17,18] GeS(Se), and SnS(Se)), C_{2h} (GaTe), and C_i ($ReS(Se)_2$).[3] The lower symmetry (D_{2h}, C_{2h}, and C_i) leads to the in-plane anisotropy, which brings one more degree of freedom than isotropic materials and delivers various physical properties.[3] Two or more LMs with similar properties can be alloyed into an additional type of 2DMs, namely, 2D alloy, which can offer tunable band gaps and the corresponding amazing electronic and optical properties.[19] These remarkable properties, including high mobility, high thermal conductivity, unique optical and mechanical properties, and high specific surface area, can be found in 2DMs, which makes them be the ideal materials for promising applications in nanoelectronics and optoelectronics devices.[20–31]

2DMs exhibit distinct electronic band structures due to the quantum confinement of electrons in 2D.[32–34] A single monolayer (1L) of 2DMs is the thinnest nanosheet exfoliated from its bulk counterpart, which can be from several micrometers to several centimeters in plane size but less than a nanometer in thickness.[1] The weak out-of-plane vdW bonding is absent in 1L 2DMs. 1L graphene (1LG) is a typical 2DM with unique properties.[13,32,35–37] The rapid progresses of graphene researches have paved the way to experimental studies on other 2DMs.[1–3,8,9,38,39] Unlike graphene, most of 1L 2DMs consist of more than one atomic element so that a single 1L of such 2DMs usually consists of more than one atomic layers in which the two nearest atoms in adjacent atomic layers are also linked via strong chemical bonds. However, two or more 1L 2DMs can be coupled with each other by Van der Waals interaction to form multilayer (ML) 2DMs in a certain stacking order. For instance, *N* layer (NL) graphenes (NLG, $N > 2$) can be stacked in a Bernal (AB) or rhombohedral (ABC) way or even a twisted way.[40–43] Exfoliated NL MX_2 can exhibit two stacking ways, *i.e.*, 2H and 3R.[44–46] Even in anisotropic NL transition metal dichalcogenides (TMDs), such as ReS_2 and $ReSe_2$, there still exist two stable categories,[47] *i.e.*, anisotropic-like (AI) and isotropic-like (IS), in terms of their stacking orders. In addition, these various 2DMs could be artificially restacked/assembled horizontally or vertically in a chosen sequence to form vdW heterostructures, which can offer huge opportunities for designing the functionalities of such heterostructures.[42,43,48–51] For a given

Dr. X.-L. Li, Dr. W.-P. Han, J.-B. Wu, Dr. X.-F. Qiao, Prof. J. Zhang, Prof. P.-H. Tan
State Key Laboratory of Superlattices and Microstructures
Institute of Semiconductors
Chinese Academy of Sciences
Beijing 100083, China
E-mail: phtan@semi.ac.cn
J.-B. Wu, Prof. J. Zhang, Prof. P.-H. Tan
College of Materials Science and Opto-Electronic Technology
University of Chinese Academy of Science
Beijing 100049, China

DOI: 10.1002/adfm.201604468

stacking order, the electronic band structures and lattice vibrations of the 2DMs are significantly *N*-dependent.[52] The band gap of 2H-MX_2 exhibits an indirect-to-direct transition from NL ($N > 1$) to 1L.[33,53,54] The NL MoS_2 field effect transistors (FETs) exhibit higher mobilities, more near-ideal subthreshold swings, and more robust current saturation over a large voltage window than 1L MoS_2.[29] The direct band gap of BP monotonically increases from bulk (0.2 eV) to 1L (1.5–2.0 eV), due to the strong interlayer coupling.[55,56] In the case of lattice vibrations, relative to 1L 2DMs, more atoms in the unit cell of NL ($N > 1$) 2DMs will result in more phonon modes in the center of Brillouin zone of corresponding phonon dispersion curves.[3,10] Each mode in 1L 2DMs will split into *N* modes in NL 2DMs, named as Davydov components, whose frequencies are determined by the interlayer coupling and the corresponding symmetry in NL 2DMs.[57,58]

The *N*-dependent electronic and optical properties of 2DMs[33,52,59] can be probed by various optical techniques, e.g., optical contrast (OC),[11,60–63] Rayleigh scattering,[64] Raman spectroscopy,[3,10,65–67] optical absorption,[68] photoluminescence (PL)[33,47,53,55] and second harmonic generation (SHG).[69–71] With increasing N, the intensity, linewidth, or lineshape of the probed optical signals of 2DM flakes can be significantly modified, and some new optical features will emerge. For instance, with increasing *N*, the PL emission from direct band gap of NL MoS_2 flakes decreases in intensity while its peak position almost keeps unchanged, however, new PL emission from indirect band gap appears for $N > 1$ and this PL peak position decreases toward lower energy with increasing *N*.[33] Considering most of 2DM flakes are deposited on substrates, such as SiO_2/Si, quartz or sapphire, the optical interference between 2DM flakes and substrate must be considered in the optical measurements, in which the SiO_2 film thickness in SiO_2/Si substrate and numerical aperture (NA) of the objective used in microscope also affect the measurement results dependently.[72]

The sensitivity of optical properties of 2DM flakes on *N* can be utilized to identify *N* of the studied 2DM flakes once the relation between spectral parameters of optical properties and *N* is determined forehand. The thickness of 2DM flakes is a serial of discrete values. The thickness of an *N* layer 2DM flake is *N* times that of monolayer 2DM flake. In principle, once *N* of the 2DM flake is identified by optical techniques, its thickness is determined. In fact, atomic force microscopy (AFM) has been widely used to measure the thickness of 2DM flakes with a precision of 5%. The tapping mode is utilized to minimize sample damage.[57,64,72,73] However, AFM technique is time-consuming and not suitable for a rapid measurement for selected spots over a large area. AFM cannot also be used for suspended samples. The different interactions of the AFM tip with the flake and substrate will lead to large thickness discrepancy for few-layer 2DM flakes.[57,64,72,73] The offset between 2DMs flake and substrate can be as large as several nanometers, but the measured height difference between two adjacent 2DM flakes is in good agreement with the corresponding thickness difference. For example, **Figure 1** shows that, the instrument offset for 1LG and 1L MoS_2 is about 1.4 and 4.0 nm, respectively. Optical techniques are fast and nondestructive techniques for the probe of physical properties of 2DM flakes. Therefore, it is necessary to construct some reliable approaches to precise identify *N* from the reported results based on optical techniques.

Ping-Heng Tan is a Professor at Institute of Semiconductors, Chinese Academy of Sciences. He obtained his BS (1996) in Physics from Peking University and PhD (2001) from Institute of Semiconductors, Chinese Academy of Sciences. He worked at Walter Schottky Institut, Technische Universität München as a Posdoc Research Associate from 2001–2003. He was a KC-Wong Royal Society Fellow at Cambridge University from 2006–2007. His current research is on the optical properties of two-dimensional materials, nanocarbon materials, and novel low-dimensional semiconductor optoelectronic materials. He was supported by the National Science Fund for Distinguished Young Scholars in 2012.

Here, we review the recent advances in the *N*-dependent optical properties of several typical 2DMs, such as NLGs, NL TMDs (e.g., 2H-MX_2 (M = Mo, W; X = S, Se), and 1T-$ReS(Se)_2$) probed by OC, Raman spectroscopy, PL, optical absorption spectroscopy, and SHG. The definite relations between the optical properties and *N* by different optical techniques have been demonstrated for rapid and accurate identification of the thickness or *N* of 2DM flakes. This review will be expected to pave the ways to construct *N*-identification techniques of 2DM flakes based on optical techniques, benefit the whole 2DM community for fundamental study, practical applications and quality appraisal for industrial products.

2. Optical Contrast

2DMs are usually transferred onto a kind of substrate, such as Si covered with a certain thickness of SiO_2 film or quartz plate, for device application purpose.[13,33] This causes a formation of multilayer structure containing air, 2DM flake and substrate. For the Si substrate covered by SiO_2, the four layered structure can be established, containing air($\tilde{n}_0$), NL 2DM($\tilde{n}_1(\lambda)$, d_1),[74] SiO_2($\tilde{n}_2(\lambda)$, d_2),[75] and Si($\tilde{n}_3(\lambda)$, d_3), where $\tilde{n}_i(\lambda)$ and d_i (i = 0, 1, 2, 3) are the complex refractive index at specific wavelength (λ) and the thickness of each medium. When white-light of a microscope is incident from air onto 2DM flakes on substrates, multiple reflections at the interfaces and optical interference within the medium of the multilayer structures will modify the reflected light intensity from 2DM flakes relative to that directly from the bare substrates. This makes the 2DM flakes can be easily seen by naked eyes *via* microscope after they are transferred onto substrates. The difference between reflected light intensity from 2DM flakes deposited on substrate and from the bare substrate is known as OC of the 2DM flakes.[11,60,61,76–78]

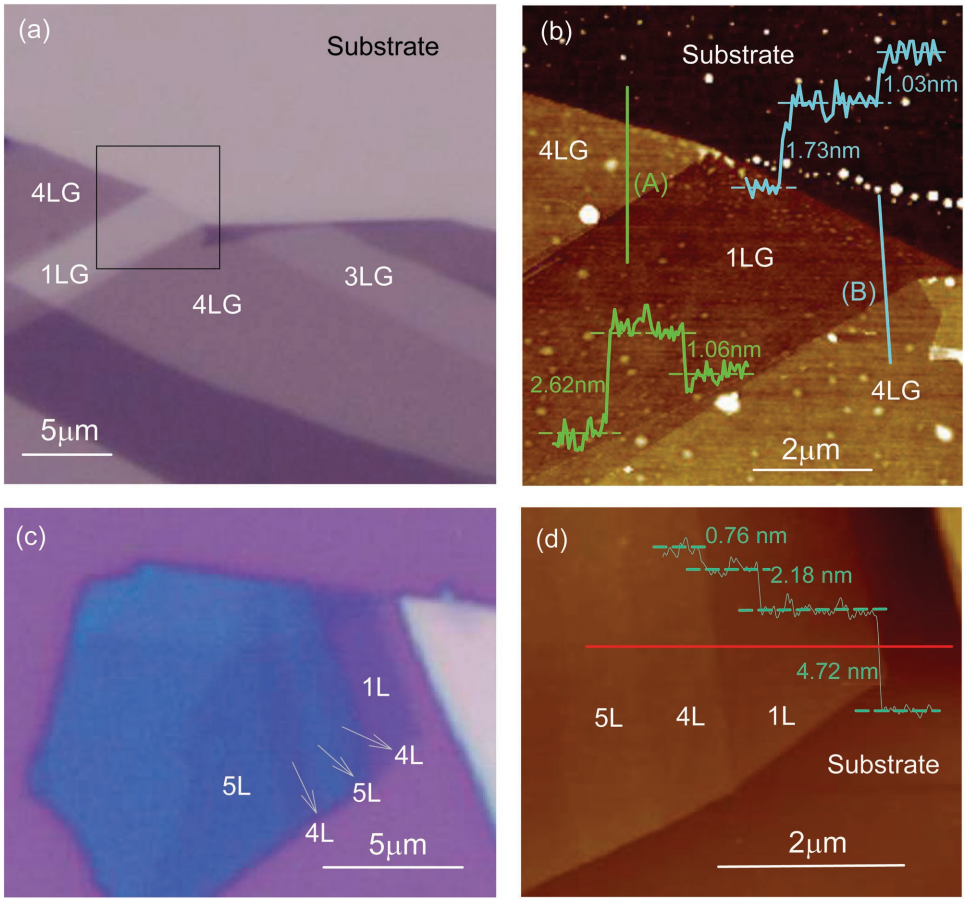

Figure 1. a) Optical image of 1LG, 3LG, and 4LG flakes. b) AFM image of 1LG and 4LG within the square frame in (a) and the flake thickness measured by AFM. The instrumental offset is ≈1.1 nm. (a,b) Adapted with permission.[72] Copyright 2015, Royal Soceity of Chemistry. c) Optical image of 1L, 4L, and 5L $MoTe_2$. d) AFM image of the samples in (c) and the flake thickness measured by AFM. The instrumental offset is ≈4.0 nm. (c,d) Adapted with permission.[57] Copyright 2012, Nature Publishing Group.

By using monochromatic illumination, 2DM flakes can be isolated from Si substrate covered with any SiO_2 thickness (h_{SiO_2}), albeit 300 nm for electronic devices and, especially, 90 nm are most suitable for its visual detection.[60,72] Because of multiple reflection interferences in the multilayer, OC of an NL 2DM flake on a substrate is dependent on the illumination wavelength λ. The 2DM flake deposited on a given substrate exhibits a distinct OC(λ), which is significantly dependent on N. Besides N, OC(λ) is also sensitive to the NA of the objective used in the microscope, which can be measured by a microscope combined with a spectrometer.

Figure 2 shows the schematic setup diagram to measure OC(λ) of 2DM flakes by a microsystem in a backscattering geometry at room temperature, which is equipped with several objectives. OC(λ) is defined as[60,61,79]

$$\mathrm{OC}(\lambda) = 1 - R_{2\mathrm{dm+Sub}}(\lambda) / R_{\mathrm{Sub}}(\lambda) \quad (1)$$

where $R_{2\mathrm{dm+Sub}}(\lambda)$ and $R_{\mathrm{Sub}}(\lambda)$ are the reflected intensities from the 2DM flakes on substrates and from the bare substrate, respectively. In some literatures, the OC(λ) also were defined as $(R_{2\mathrm{dm+Sub}}(\lambda)\text{-}R_{\mathrm{Sub}}(\lambda))/(R_{2\mathrm{dm+Sub}}(\lambda) + R_{\mathrm{Sub}}(\lambda))$.[11] Here, we use the definition from Equation (1). Tungsten halogen lamp can be used as a light source for reflection spectra measurement. The insets of Figure 2 show the measured $R_{2\mathrm{dm+Sub}}(\lambda)$, $R_{\mathrm{Sub}}(\lambda)$ and calculated OC(λ) by Equation (1) for 2LG on SiO_2/Si substrate (h_{SiO_2} = 90 nm), respectively. OC(λ) can be quantitatively calculated by the multiple reflection interference method[60,61,79,80] once the refractive index of 2DMs is known. The transfer-matrix method can be used to calculate theoretical OC(λ),[79,80] where the electric and magnetic field components in each medium are associated by multiplication of some characteristic matrices, dependent on the angle of light, the medium thickness and the complex refractive index of each medium. To reach a good agreement with the experimental data, the NA of the objective has to be considered. Because the incident and reflective lights are collected by the same microscope objective with a given NA, all of the lights with an inclined angle in the field of objective rather than the lights only vertical to the NLG should be considered. Thus, the s-polarization (the incident light is polarized with its electric field perpendicular to the plane containing the incident) and p-polarization (the incident light is polarized with its electric field parallel to the plane of incidence) components should be treated separately in calculation.[80] Details of calculation has been provided in Lu et al.[80]

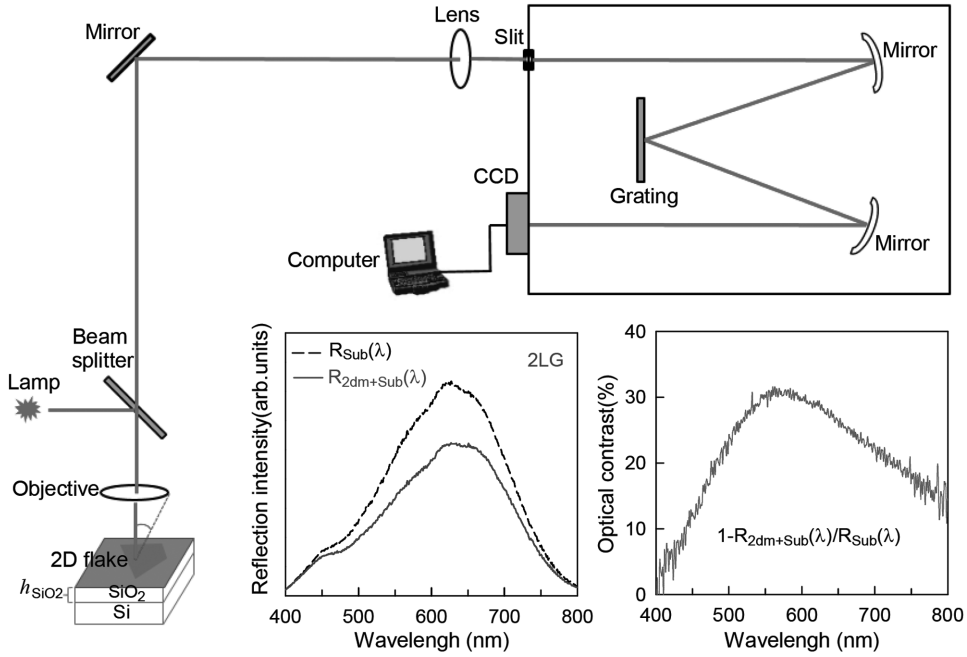

Figure 2. Schematic diagram of the microscope system to measure OC(λ). For characterizing small flakes (few microns), a pinhole is needed to inset between the lamp and objective in order to collect the reflection only from the desired flake for a nonconfocal system. The collected reflection spectra from bare SiO_2/Si substrate (h_{SiO_2} = 90 nm) and from 2LG deposited on substrate are shown in the inset (a) as $R_{Sub}(\lambda)$ and $R_{2dm+Sub}(\lambda)$, respectively. The experimental OC(λ) = 1 − $R_{2dm+Sub}(\lambda)/R_{Sub}(\lambda)$ is depicted in the inset (b).

Figure 3a shows the experimental OC(λ) values of a 10LG flake deposited on SiO_2/Si substrate (h_{SiO_2} = 89 nm) using objectives with NA = 0.25, NA = 0.45, and NA = 0.90, respectively. The maximum value of OC(λ) with NA = 0.90 is apparently smaller than those with NA = 0.25 and NA = 0.45, and the peak position exhibits a shift between any two of OC(λ). The experiments show that there exists a significant discrepancy between experimental and theoretical OC(λ) for NA = 0.90[80] because the objective lens is not totally filled by incident light thus leading to a smaller effective NA.[64,79] The objective with NA ≤ 0.55 is recommended to reach a good agreement between experimental and theoretical

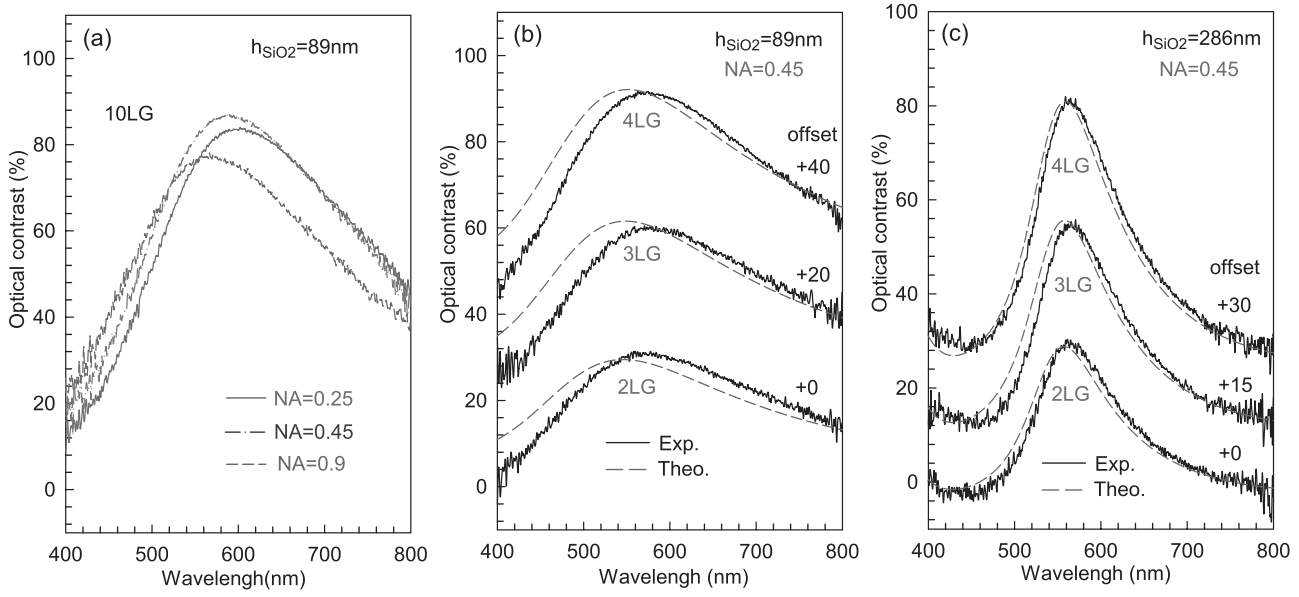

Figure 3. a) The experimental OC(λ) values of a 10LG flake deposited on SiO_2/Si (h_{SiO_2} = 89 nm) using objectives with NA = 0.25, NA = 0.45, and NA = 0.90, respectively. The experimental OC(λ) and the calculated results of 2LG, 3LG, and 4LG for b) h_{SiO_2} = 89 nm and c) h_{SiO_2} = 286 nm (c), NA = 0.45.

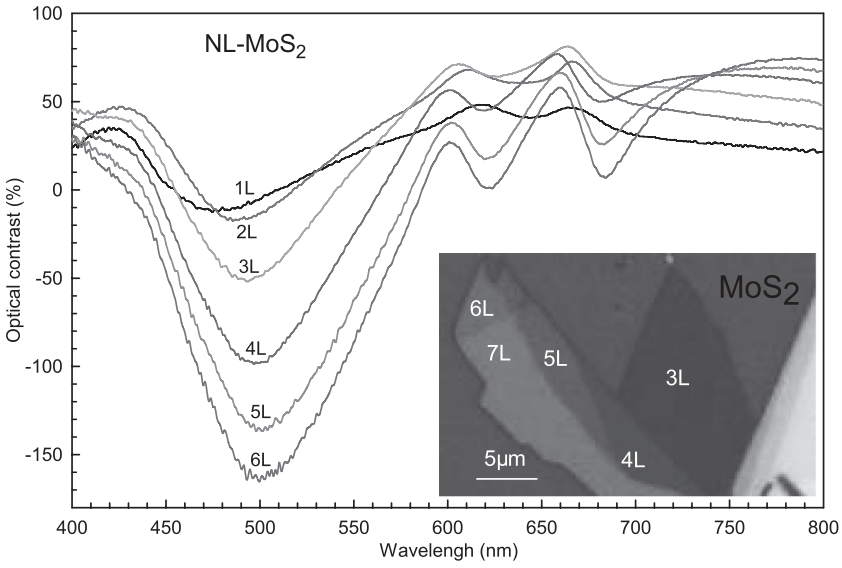

Figure 4. The experiment OC(λ) of 1-6L MoS_2. The inset shows the optical image of a flake with 3-7L MoS_2.

OC(λ).[80] Indeed, For NA = 0.45, the experimental OC(λ) of 2LG, 3LG, and 4LG for both h_{SiO_2} = 89 nm (Figure 3b) and h_{SiO_2} = 286 nm (Figure 3c) are in accordance with the theoretical ones calculated by transfer-matrix method in the broad range of 400–800 nm.

In general, OC(λ) of 2DM flakes on SiO_2/Si substrates is significantly dependent on N, NA, and h_{SiO_2}. For 2DMs with a unified complex refractive index ($\tilde{n}(\lambda)$) from monolayer to multilayer, such as NLG, once h_{SiO_2} and NA ($\leq$ 0.55) are given, the experimental OC(λ) is found to be in good agreement with the theoretical ones. Therefore, OC(λ) can be adopted to identify N of 2DM flakes with a unified $\tilde{n}(\lambda)$), such as NLG. At first, to determine h_{SiO_2} by spectroscopic ellipsometer[81] or OC[80]; second, to measure OC(λ) of the 2DM flake with NA ($\leq$ 0.55); third, to calculate OC(λ) of NL 2DM flakes using known NA, h_{SiO_2} and $\tilde{n}(\lambda)$; finally, to check which N of the theoretical OC(λ) for NL 2DM flakes is close to the experimental OC(λ) and determine N. Due to the advantages such a simple, efficient, nondestructive, and unnecessary of expensive and nonstandard equipment, OC technique is regarded as a good option for thickness or N identification of NLG.[60,61,79,80] The accuracy of N identification depends on the OC(λ) difference between two flakes with adjacent N. The OC technique can be used to identify NLG up to N = 8.

Because absorption properties[54,82] of ultrathin TMD flakes are significantly N-dependent in the visible range due to the presence of exciton effect, ultrathin TMD flakes are lack of a unified $\tilde{n}(\lambda)$ from monolayer to multilayer. **Figure 4** shows the experimental OC(λ) of 1-6L MoS_2, which are also dependent on h_{SiO_2} and NA. It is obvious that no common spectral features can be found within them. Therefore, it is hard to theoretically reproduce OC(λ) of TMD flakes with specific N to determine N for TMD flakes by comparing them with the experimental ones.

The 2DM flakes with different N usually display different colors in the optical images. Li et al.[63] have given the color difference values between 1-15L 2DMs and substrate, including graphene, MoS_2, WSe_2, and TaS_2, on SiO_2/Si substrates (h_{SiO_2} = 90 or 300 nm). These data were obtained from the brightness profile of color images or grayscale images of the red (R), green (G), or blue (B) channel in samples and substrates, can be affected by illumination source, white balance, NA and h_{SiO_2}. Because it is difficult to establish a relation between the color difference and N for any NA and h_{SiO_2}, it cannot be used to accurately identify N of 2DM flakes for common conditions with any white balance, NA and h_{SiO_2}.

3. Rayleigh Scattering

Rayleigh scattering is the elastic scattering of light by particles much smaller than the wavelength of the radiation. The particles can be individual atoms. Under backscattering configuration, the scattered signal with same frequency as the laser excitation is the elastically scattered photons from Rayleigh scattering. The setup depicted in Figure 2 can be used to measure Rayleigh signal once the lamp and spectrometer are replaced by a laser beam and a photon-counting avalanche photodiode, respectively.

Casiraghi et al.[64] have first given the Rayleigh scattering contrast method, as shown in **Figure 5**a,b. Figure 5a shows an optical image of 1-3LG and 6LG prepared from micromechanical exfoliation of graphite and deposited on a SiO_2/Si substrate (h_{SiO_2} = 300 nm). Rayleigh scattering is performed with an inverted confocal microscope where a He–Ne laser (633 nm) is used as the excitation source. Confocal Rayleigh images are obtained by raster scanning the sample. Figure 5b shows the 3D confocal Rayleigh map for the NLG sample shown in Figure 5a. Rayleigh contrast was also estimated by Equation (1). The Rayleigh contrast appears to increase with N in certain wavelength ranges.[64] Rayleigh scattering can also be applied to the NLG flakes grown by chemical vapor deposition (CVD), which are transferred onto the SiO_2/Si substrate (h_{SiO_2} = 90 nm).[83] Figure 5c shows the optical image of an CVD-grown flake, and its Rayleigh contrast mapping obtained by the 532 nm laser is shown in the Figure 5d. It is found, the closer the measured spot is to the center of the CVD-grown flake, the higher the Rayleigh contrast is. This results from more graphene layers grown at the flake center.

Because that multiple reflection interferences of both the laser beam and Rayleigh signal still occur in the multilayer containing air, 2DM flakes and substrate, the theoretical value of Rayleigh contrast can also be calculated by the matrix transfer method.[64] By comparing the experimental Rayleigh contrast of a 2DM flake with the theoretical one of 2DM flakes with different N, one can identify N of NLG flakes. For example, for a CVD-grown multilayer graphene (MLG) flake, each graphene region with a definite N in the Figure 5c was distinguished by the Rayleigh contrast mapping and was marked in the Figure 5d.

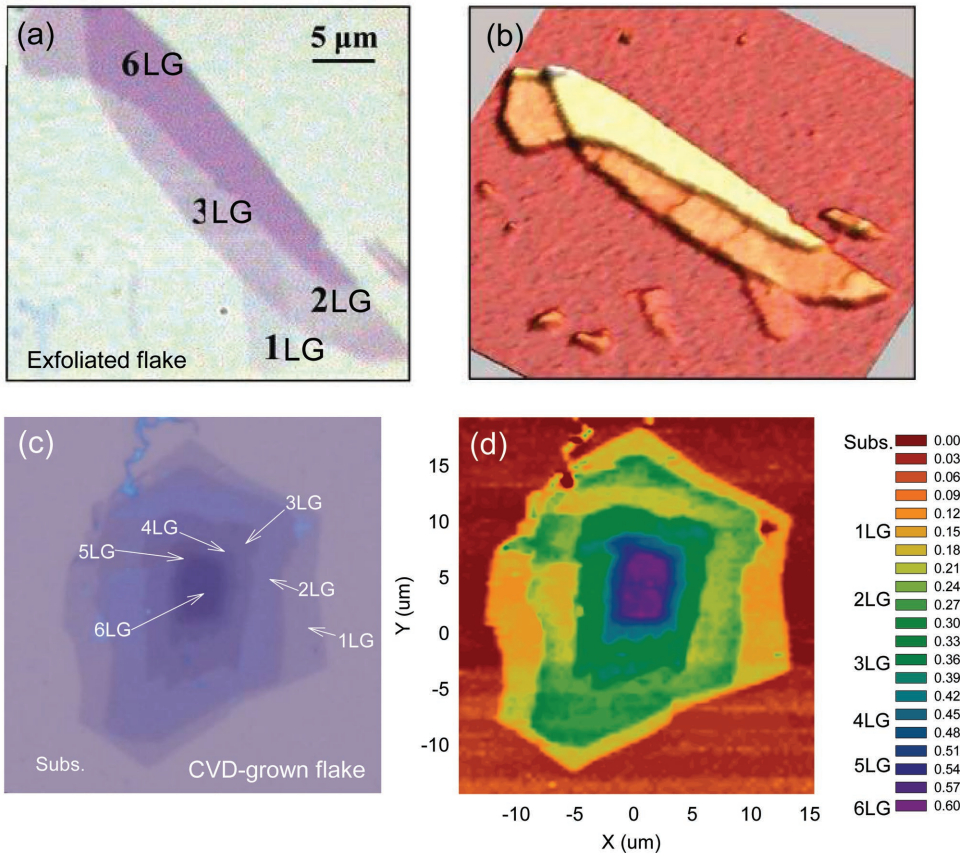

Figure 5. Optical image of a) NLG with 1-3LG and 6LG prepared from micromechanical cleavage and the corresponding 3D confocal Rayleigh imaging of b) NLG flakes by 633 nm excitation. Reproduced with permission.[64] Copyright 2007, American Chemical Soceity. Optical image of c) CVD-grown NLG flakes and the corresponding Rayleigh contrast mapping of d) the CVD-NLG flakes by 532 nm excitation from which N of NLG flakes in different regions is determined.

Because the laser excitation can be used for Rayleigh scattering, the spatial resolution of the Rayleigh contrast is much better than that of OC measured by a collimated white-light beam. The spatial resolution of Rayleigh contrast can be down to the size of the laser spot. In fact, the measured Rayleigh contrast by a laser source is a monochromatic OC with a wavelength equal to that of the laser source. Therefore, to obtain a good Rayleigh contrast mapping, one should choose the laser excitation with an optimal wavelength at the maximum of OC(λ), e.g., ≈550 nm for NLG when h_{SiO_2} = 90 or 300 nm. For NL MoS_2, the optimal wavelength is ~500 nm, as shown in the Figure 4. Around this wavelength, OC of NL MoS_2 flakes are much sensitive of N than other wavelengths.

4. Raman Spectroscopy

Raman spectroscopy is the prime nondestructive characterization tool to probe the physical properties, such as phonons, electron–phonon coupling (EPC), band structures and interlayer coupling of 2DMs.[10,65,84] Raman spectra of 2DMs consists of high- and ultralow-frequency Raman modes. The high-frequency modes are generally from in-plane vibrations, such as D, G, and 2D mode in NLG[84] and E^1_{2g} and A_{1g} modes in NL MX_2.[10] The ultralow-frequency (ULF) modes correspond to the relative motions of the planes themselves, either parallel or perpendicular to the plane, such as the shear (S) modes[67,85] and the layer-breathing (LB) modes,[85] which are related to the interlayer coupling. Moreover, the Si mode from SiO_2/Si substrate underneath NL 2DMs is hardly modified by defects and disorders in NL 2DMs, however, its intensity will be affected by the thickness of 2DMs.[72,86] High-frequency (HF) and ULF modes of 2DMs and Raman modes from substrates can be strongly dependent on N in the peak position, profile, linewidth, and new HF and ULF modes will appear in the Raman spectra of 2DMs.

4.1. HF Raman Modes of 2DMs

4.1.1. N-Dependent Frequency

HF Raman modes have been deeply investigated in NLG and graphite materials, providing useful information on the defects (by D band), in-plane vibration of sp^2 carbon atoms (by G band) as well as the stacking order (by 2D band). The HF Raman spectrum of the intrinsic NLG consists of G (≈1580 cm^{-1}) and 2D (≈2670 cm^{-1}) modes.[66,84] The G peak originates from

in-plane vibration of sp^2 carbon atoms and is due to the doubly degenerate zone center E_{2g} mode. The 2D band is the second order of the D peak, where D peak comes from TO phonons around the Brillouin Zone edge near K, is active by double resonance process.[84] Because the interlayer coupling is much weaker than the intralayer C—C bonding, the interlayer coupling almost does not affect the intralayer C—C bonding in NLG. Therefore, it is revealed that the peak position (or frequency) of the G mode, Pos(G), is almost insensitive to N.[67] However, the profile of the 2D mode is strongly dependent on N of NLG. Here, we will first discuss the 2D profile of AB-stacked NLG as a function of N.

Because the 2D band originates from a two-phonon double resonance Raman process, it is closely related to the band structure of graphene layers. 1LG has a single and sharp 2D band, but the 2D band of NL graphenes can be fitted by multiple Lorentzian peaks, due to the multiple resonance Raman processes related with the electronic band structure of NLGs. Ferrari et al.[66] have successfully explained the changes of the 2D band in shape, linewidth, and peak position for graphene and graphene layers. The 2D mode is dispersive.[41,87] The Pos(2D) and line shape of 2D mode depend on the excitation energy. Zhao et al.[87] have demonstrated that the changes of the 2D bands can be used to clearly identified 1LG and 2-4LG with AB stacking once the excitation wavelength is 633 nm. The Raman spectra of 1-5LG measured with 633 nm laser excitation are shown in **Figure 6**.[87] The 2D bands of AB-stacked 2LG, 3LG and 4LG can be fitted with 4, 7, 8 Lorentzian peaks, respectively. The characteristic peaks of each band are shown by the arrows, stars and pluses. However, for more than five graphene layers, the difference between their Raman spectra is insufficient to accurately distinguish them. Because the different components of the 2D bands may exhibit different resonant behaviors dependent on laser wavelength, it is very important to choose an appropriate laser wavelength to identify N of NLG.[87] Moreover, the line shape of 2D mode also depends on the stacking order of graphene.[41] For example, the 2D peak of ABC-stacked 3LG under excitation of 633 nm also can be fitted by seven Lorentzian peaks like as that of AB-stacked 3LG, however, the clear blueshifts of the subpeaks, especially those of higher frequencies for the ABC-stacked 3LG probe the difference of band structure between AB- and ABC-stacked 3LG.[41,88] The 2D band of ABC-stacked NLG also shows an N-dependent behavior.[40,41,88]

2H-MX_2 is a subject of intense researches because of its electronic and optical properties, such as strong PL,[33,53] electroluminescence (EL),[89] controllable valley and spin polarization.[90–92] A 1L MX_2 consists of two planes of hexagonally arranged X atoms linked to a hexagonal plane of M atoms *via* covalent bonds. In the NL MX_2, individual MX_2 layers are held together by weak vdW forces. The change of symmetry and atoms in unit cell with *N* and the presence of interlayer coupling in NL MX_2 ($N > 2$) make the high-frequency modes of NL MX_2 be dependent on *N*.

Figure 7a,b shows the high-frequency Raman spectra of 1-10L MoS_2 measured by 532 nm excitation and that of 1-8L WS_2 under 488 nm excitation, respectively. The high-frequency Raman spectra of bulk MX_2 consist mainly of the E^1_{2g} and A_{1g}

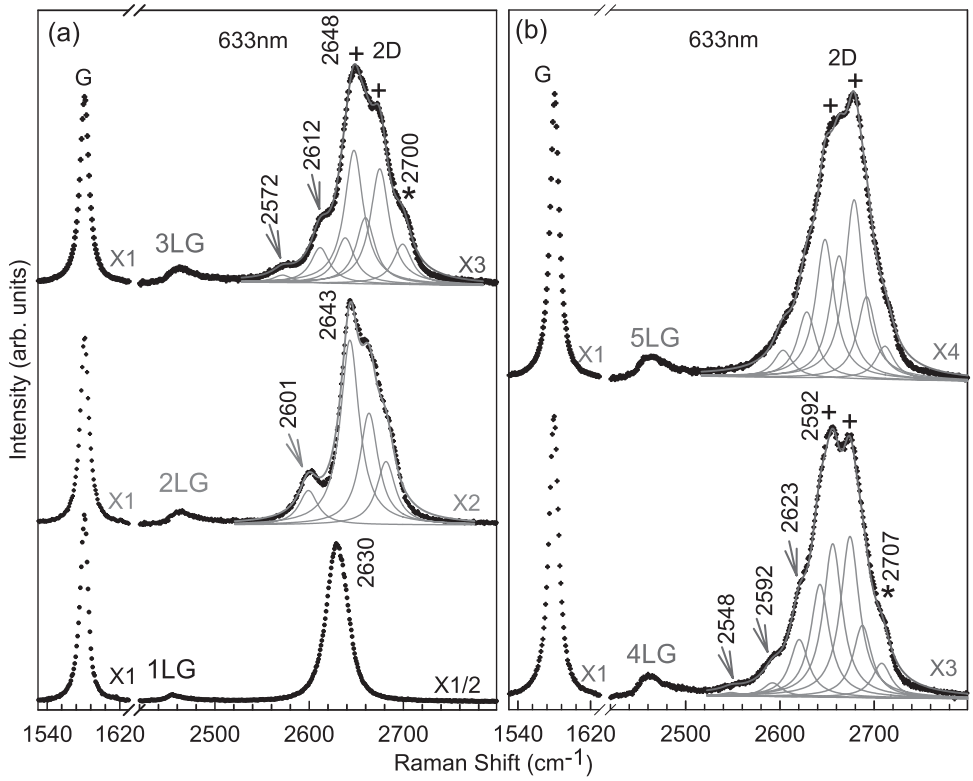

Figure 6. Raman spectra of a) G and 2D peaks of 1-3LG and b) those of 4LG and 5LG excited by the 633 nm laser. (a–b) Adapted with permission.[87] Copyright 2010, APS.

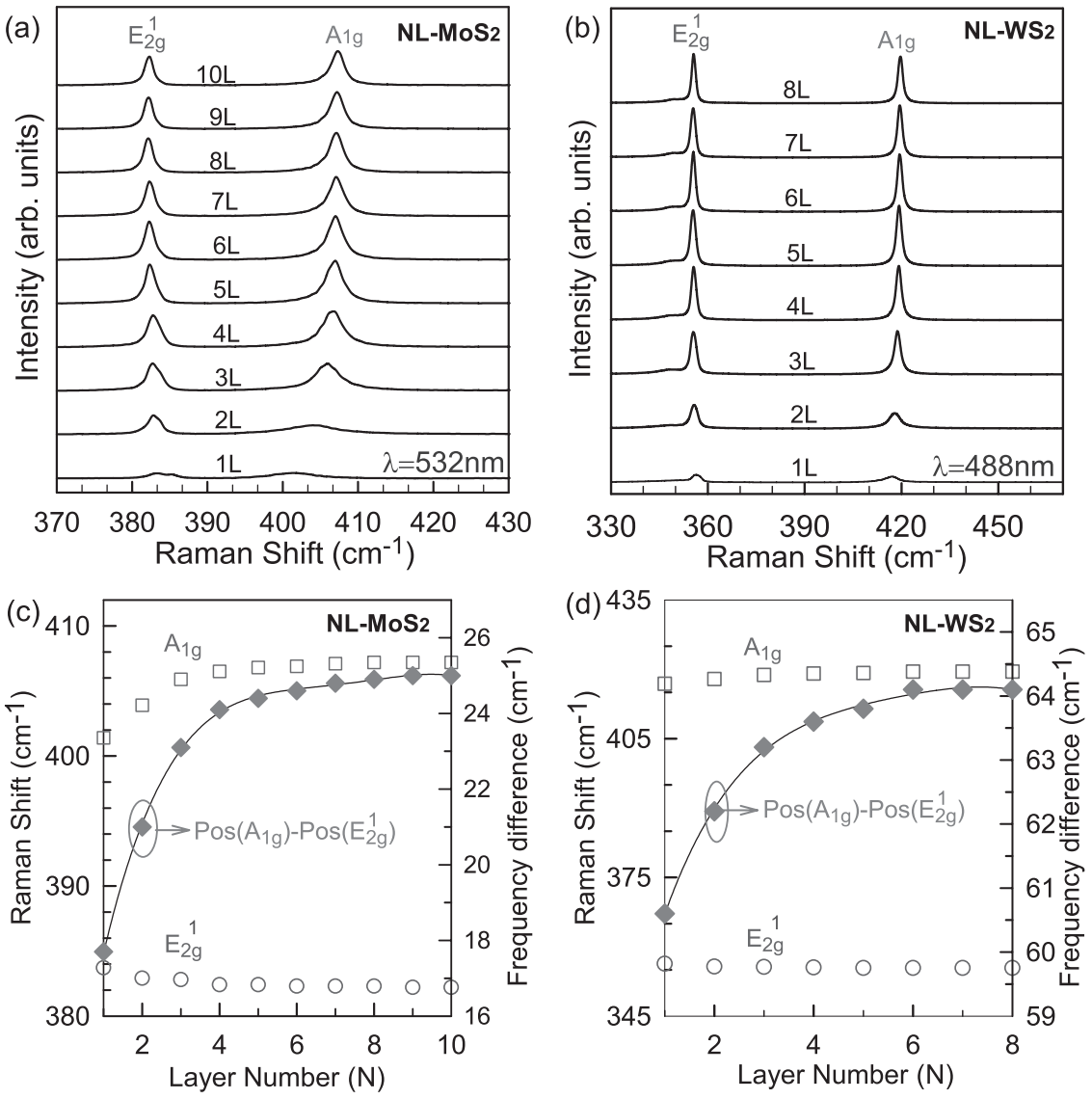

Figure 7. HF Raman modes of 1-10L MoS_2 a) measured by 532 laser and those of 1-8L WS_2 b) at 488 laser. The frequency of the E^1_{2g} and A_{1g} modes and their difference with increasing N of c) NL MoS_2 and d) NL WS_2.

modes. Because of the different symmetries between even and odd NL MX_2 and bulk MX_2, these two modes in bulk MX_2 should be assigned as the E′ and A'_1 in odd NL (ONL) MX_2 and the E_g and A_{1g} modes in even NL (ENL) MX_2,[10,59,93] respectively. However, to see the evolution from 1L to NL ($N > 1$), hereafter the two modes for all cases are simply labeled as E^1_{2g} and A_{1g}, as commonly done in the literatures.[10,94–96] Figure 7a shows that E^1_{2g} and A_{1g} mode is respectively located at ~380 and ~402 cm^{-1} in MoS_2. With increasing N, the frequency of the E^1_{2g} mode, Pos(E^1_{2g}), decreases and that of the A_{1g} mode, Pos(A_{1g}), increases. The frequency difference $\Delta\omega(A - E)$ = Pos(A_{1g}) − Pos(E^1_{2g}) increases from 17.4 cm^{-1} for 1L to 25 cm^{-1} for 10L, following the formula of $\Delta\omega(A - E) = 25.8 - 8.4/N$,[10] as shown in Figure 7c. The different trend of Pos(E^1_{2g}) and Pos(A_{1g}) with N is attributed to the surface effect as the larger force constants at the surface of the thin film can make a difference.[97] It is found that the nearest vdW interactions can significantly affect the frequency of the HF phonon modes in NL MX_2.[57]

Similar anomalous frequency difference between the E^1_{2g} and A_{1g} modes with increasing layer number also exists in other 2D MX_2. However, the E^1_{2g} and A_{1g} modes of WS_2 are found to be not so sensitive to N.[98,99] Figure 7d shows that E^1_{2g} and A_{1g} mode is respectively located at ≈356 and ≈419 cm^{-1} in WS_2. The frequency shift of both E^1_{2g} and A_{1g} modes for NL WS_2 (shown in Figure 7d) is less than 3 cm^{-1}. The case of E^1_{2g} and A_{1g} modes in WSe_2 is more complicated. E^1_{2g} and A_{1g} modes overlap each other at ≈248 cm^{-1}. The E^1_{2g} mode is very weak and can be revealed under cross (HV) polarization configuration according to polarization properties of E_{2g} peak observable under both the parallel (VV) and HV polarization configuration while A_{1g} observable under VV polarization configuration.

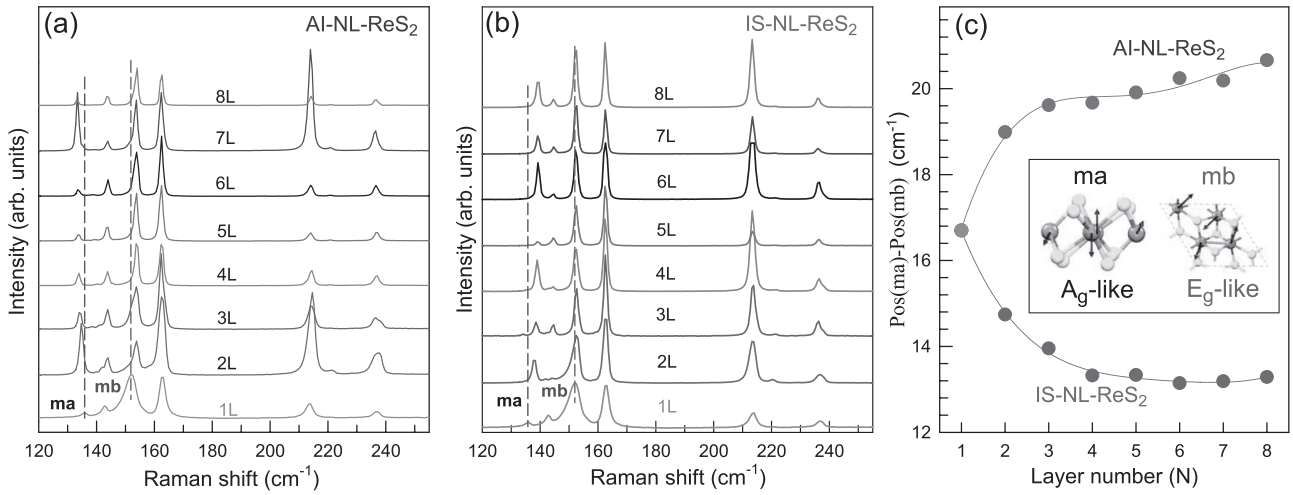

Figure 8. HF Raman spectra of a) AI- and b) IS-NL-ReS_2 up to 8L in the range of 120–250 cm^{-1}. c) Pos(mb)-Pos(ma) as a function of N for AI-stacked (green circles) and IS-stacked 2–8L ReS_2. The inset shows the atom displacement of the modes ma and mb. Reproduced with permission.[47] Copyright 2016, Royal Soceity of Chemistry.

Anisotropic 2DMs, such as ReS_2, offer one more dimension than isotropic 2DMs to tune their physical properties. The bulk and 1L ReS_2 belong to the C_i space group. The crystal structure of ReS_2 is much more complicated than graphene and MX_2. Its unit cell contains four formula units consisting of two categories of Re atoms together with four categories of S atoms. Each Re has six neighboring S sites, and the Re atoms are sandwiched by the S atoms at both sides. Because the unit cell of 1L ReS_2 comprised 12 atoms, it has 36 normal vibrational modes. The Γ phonons of 1L ReS_2 can be expressed by the irreducible representations of C_i as follows: $\Gamma = 18(A'' + A')$.[47,100,101] In principle, for the NL ReS_2 with a unit cell of 12N atoms, 36N modes are expected. There are two stable stacking orders, namely isotropic-like (IS) and anisotropic-like (AI), in the NL ReS_2.[47] We summarize the high-frequency Raman spectra of AI- and IS-NL-ReS_2 up to 8L from a range of 120–250 cm^{-1} in **Figure 8**a,b, respectively, together with that of 1L ReS_2 for comparison.[47] The number of modes does not significantly change with N increasing from 1L to 8L. The relative intensity between different modes is usually sample dependent, owing to the relative orientation between NL ReS_2 crystal axis and laser polarization direction. The peaks at ≈161, ≈213, ≈235 cm^{-1} do not appreciably move with respect to N for both AI- and IS-NL-ReS_2. However, as marked by the dashed lines in Figure 8a,b, the ma and mb peaks have different *N*-dependent evolution tendencies in AI- and IS-NL-ReS_2. The vibrational displacements of ma and mb mode are A_g-like out-of-plane and E_g-like in-plane mode, respectively, analogous to those in NL MX_2. The ma mode of 1L ReS_2 softens in AI-stacked NL ReS_2 while it stiffens for IS-stacked ones. Unlike the ma mode, the mb mode stiffens in AI-stacked NL ReS_2 but almost remains unmoved for all IS-stacked samples. Consequently, $\Delta\omega(mb - ma)$ = Pos(mb)–Pos(ma) increases from 16.7 cm^{-1} of 1L ReS_2 to 20.6 cm^{-1} of AI-8L-ReS_2, but decreases to 13.3 cm^{-1} of IS-8L-ReS_2, as plotted in Figure 8c.

All the 2DM flakes are bonded together by the vdW coupling. The HF Raman peaks of NL 2DM flakes should always exhibit frequency shifts from bulk to monolayer, either significantly or insensitively dependent on *N*. Once the frequency of HF modes or frequency difference between two HF modes of NL 2DM flakes is sensitive to *N*, it can be applied for *N* identification for 2DM flakes, such as the position and profile of the 2D modes in NLG, Pos(A_{1g})-Pos(E^1_{2g}) in NL MoS_2 and $\Delta\omega(mb - ma)$ in NL ReS_2. However, for almost all the 2DM flakes, when $N > 5$, the frequency difference of HF modes between NL and (N+1)L 2DM flakes, so in this case, it is no longer valid for N identification. The HF Raman peaks always exhibit frequency shifts from bulk to monolayer, which has been observed in other 2DMs, such as Bi_2Se_3, Bi_2Te_3, PtS_2, WTe_2, GaS, and GaSe.[3,11,102–104]

4.1.2. N-Dependent Peak Intensity

In the simplest model, the Raman intensity of HF modes in NL 2DMs would increase with N, because there are more 2D layers to contribute the Raman signal. However, the thicker 2DM flake also causes the stronger absorption of the laser beam and Raman signal. Thus, after a critical *N*, the Raman intensity of HF modes in NL 2DMs would decrease with *N*.

Again, we take NLG as an example. 22 intrinsic NLG flakes with *N* from 1 to 102 are deposited on (different) SiO_2/Si substrates (h_{SiO_2} = 89 nm) by mechanical exfoliation. The thickness of NLG flakes was pre-estimated by the AFM measurement. Considering that the real NLG may be defective, after the above measurement, defects were introduced intentionally for all the NLG flakes by ion implantation. The peak area of the G mode, I(G), is also measured on the defective NLG flakes, which is normalized by that of the Si peak from bare substrate, I_0(Si). The schematic diagram for Raman measurements is shown in **Figure 9**a. After the ion implantation, the D peak at ≈1350 cm^{-1} appears in the Raman spectra of the NLG flakes, as depicted in Figure 9b, meaning that the NLG flakes become defective. The trend of $I(G)/I_0(Si)$ as a function of *N* for intrinsic and defective NLG flakes is similar to each other, so only *N*-dependent $I(G)/I_0(Si)$ in the defective NLG flakes at

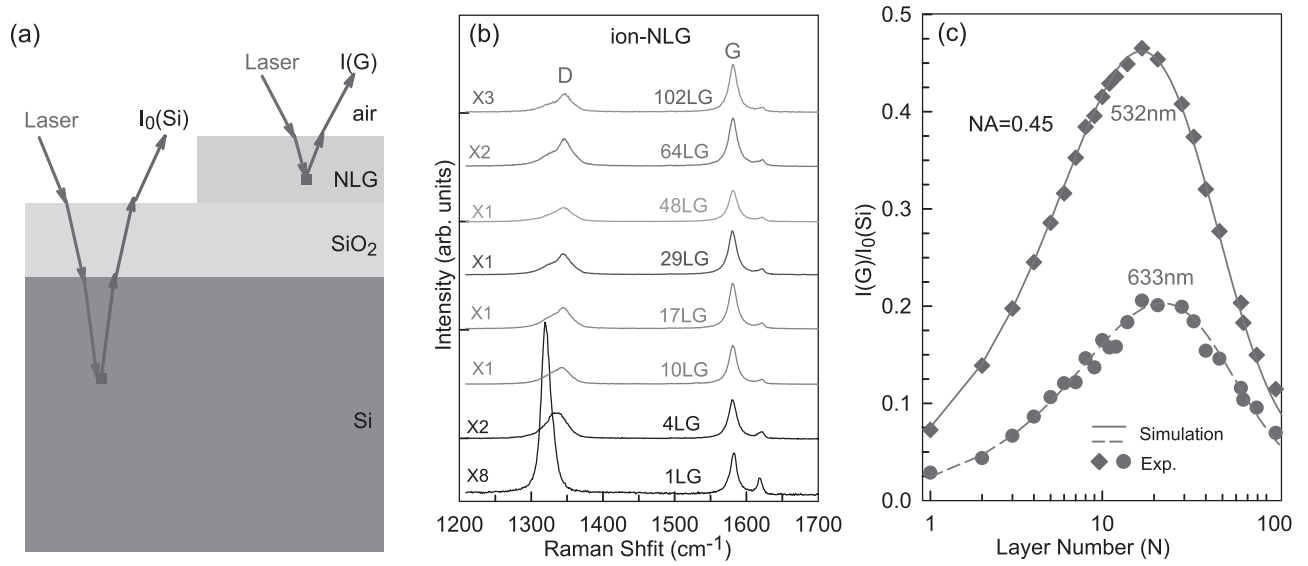

Figure 9. a) Schematic diagram to measure the Raman intensity of the Si mode from bare SiO_2/Si substrate (denoted as I_0(Si)) and of the G mode from NLG (denoted as I(G)). b) Raman spectra of defective NLGs with a few N in the range of the D and G peaks. The excitation wavelength is 633 nm. c) The experimental and theoretical $I(G)/I_0(Si)$ as a function of N of NLG flakes. The excitation wavelengths of 532 and 633 nm are used. The objective NA is 0.45. Adapted with permission.[72] Copyright 2015, Royal Society of Chemistry.

excitation wavelengths of 532 and 633 nm are summarized in the Figure 9c. As expected, $I(G)/I_0(Si)$ first increases to a maximum when N increases up to N~18 and then decreases with increasing N.[72]

N-dependent $I(G)/I_0(Si)$ can be simulated based on the multiple reflection interference model in air/NLG/SiO_2/Si multilayers.[72,73,105,106] This model is used similar to the case to calculate OC of NLGs on SiO_2/Si substrate. However, when we calculate the Raman intensity from a multilayer structure, the multiple reflections and optical interference of the laser beam and Raman signal must be treated separately to calculate the corresponding enhancement factors. Given that the different polarization dependence of the Raman modes of NLG and Si substrates due to their different lattice symmetries, the Raman tensor **R** of the phonon mode for NLG and Si must also be considered. The ratio (η) of Raman scattering efficiency between silicon and carbon atoms is used as an adjustable parameter to fit the experimental $I(G)/I_0(Si)$ in Figure 9c. Finally, the theoretical $I(G)/I_0(Si)$ is found to be in good agreement with the experimental ones in the defective NLGs and η is fitted as 0.26 and 1.68 for the 532 and 633 nm laser excitations, respectively. Details of calculation has been referred in Li et al.[72]

$I(G)/I_0(Si)$ of NLGs is not monotonically dependent on N, however, the case is different if I(G) is normalized by the peak area of the Si mode from SiO_2/Si substrate beneath the NLG (denoted as I_{2dm}(Si)). The laser beam will first reach down to the Si substrate after the absorption by NLG flakes, and the Raman signal from Si substrates will be absorbed again by NLG flakes before it is collected by the objective. Therefore, I_{2dm}(Si) decreases monotonically with increasing N. The Schematic diagram to measure I(G) and I_{2dm}(Si) is demonstrated in **Figure 10**a. Figure 10b shows the Si mode from the SiO_2/Si substrate beneath the NLG flake and the G mode from intrinsic NLGs with specific N. Once I(G) of the NLG flakes is normalized by the corresponding I_{2dm}(Si), $I(G)/I_{2dm}(Si)$ increases monotonically with increasing N, and $\mathrm{Log}(I(G)/I_{2dm}(Si))$ is almost linearly dependent on Log(N), as shown in Figure 10c.[72] The experimental N-dependent $I(G)/I_{2dm}(Si)$ can be well reproduced by the theoretical simulation by the multiple reflection interference model as discussed above.[72,73,105,106]

Similar to NLG, $I(E^1_{2g})$ and $I(A_{1g})$ in NL MX_2 are also dependent on N.[94,99] Taking NL MoS_2 as an example, $I(E^1_{2g})/I(Si_0)$ and $I(A_{1g})/I(Si_0)$ first increase up to $N = 4$ and then decrease with increasing N.[86] Its critical N is much smaller than the case in NLG, because NL MX_2 exhibits stronger absorption above its band gap than NLG. Besides NLG and NL MX_2, the N-dependent Raman intensity of HF modes also can be observed in other 2DMs, such as BP and $ReSe_2$.[107,108]

Because N-dependent $I(G)/I_0(Si)$ and $I(G)/I_{2dm}(Si)$ for NLGs deposited on SiO_2/Si substrate can be well simulated by the multiple reflection interference model, $I(G)/I_0(Si)$ and $I(G)/I_{2dm}(Si)$ can be applied in the N determination of the NLG flakes. However, there exist two problems for such protocol: 1) the fitting parameter η is excitation-wavelength dependent, which must be determined for each laser wavelength before application for N determination; 2) I_0(Si) and I_{2dm}(Si) is related with the crystal orientation of Si substrates if the Si (111) is not used in the SiO_2/Si substrates. To construct the relation between N and I(G) normalized by I_0(Si) or I_{2dm}(Si) for N determination, it is better to use the same SiO_2/Si substrate, whose crystal orientation must be kept as the same with each other during the intensity measurement for each Raman system.

The above protocol cannot be applicable to 2DMs whose $\tilde{n}(\lambda)$ is not unified from monolayer to multilayer, such as ultrathin TMD flakes. Because HF mode intensity usually is sensitive to the doping level,[109] disorder level[110] and stacking orders,[42] the above protocol cannot be also applicable to highly doped, heavily disordered, or randomly stacked 2DMs.

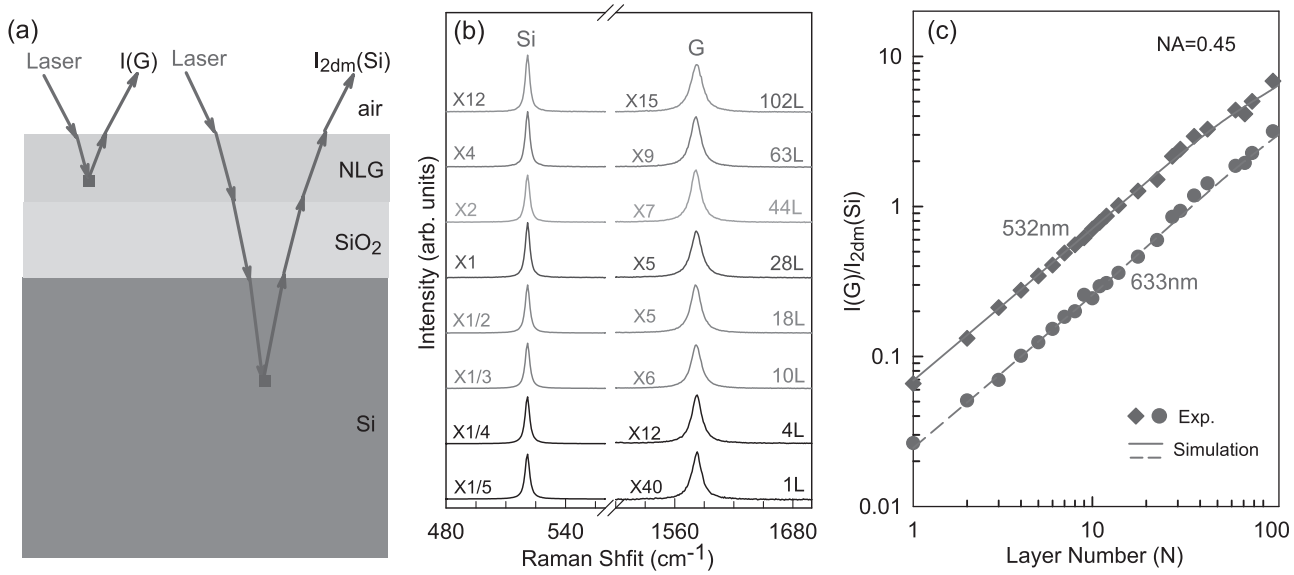

Figure 10. a) Schematic diagram to measure I(G) of NLG and I_{2dm}(Si). b) The Si mode from the SiO_2/Si substrate beneath the NLG flake and the G mode from intrinsic NLGs with specific N. The excitation wavelength is 633 nm. c) The experimental and theoretical $I(G)/I_{2dm}(Si)$ as a function of N. The objective NA is 0.45. The excitation wavelengths of 532 and 633 nm are used. Adapted with permission.[72] Copyright 2015, Royal Society of Chemistry.

4.2. ULF Raman Spectroscopy

Because the interlayer coupling in multilayer 2DMs is mainly the weak vdW interactions, the frequencies of Raman modes relevant with the interlayer coupling is very low and usually is below 100 cm^{-1}. There are two types of interlayer vibration modes, the shear modes and layer-breathing modes, which correspond to the relative motions of the atom planes parallel and perpendicular to the plane, respectively. The shear mode is referred to as the *C* mode in (twisted) MLG because it provides a direct measurement of the interlayer coupling and was first observed in MLG.[67] As for a general notation for interlayer vibration modes in LMs, we denote the shear and layer breathing modes as the S and LB modes, respectively. The S and LB modes do not exist in monolayer 2DMs. The S or LB modes are also not expected in bulk LMs which have only one rigid layer in its unit cell (for example, ReS_2, $ReSe_2$ and Bi_2Se_3). The S and LB modes have been observed in multilayer graphene,[67,111] TMDs,[47,85,107,112] Bi_2Se_3,[102] BP,[113,114] PtS_2,[103] and so on.

In an NL 2DMs, there are N-1 S and N-1 LB modes, which are denoted as S_{NN-i} and LB_{NN-i} (i = 1, 2, ..., N-1), where the S_{N1} (LB_{N1}) (i.e., $i = N$-1) is the one with highest frequency and C_{NN-1} (LB_{NN-1}) (i.e., $i = 1$) is the one with lowest frequency. The frequencies of these modes are linked with N by a linear chain model (LCM) in which each atom layer is considered as a single ball and there is mutual coupling between them.[67] In general, only the nearest-neighbor interlayer interaction can be considered for LCM to describe *N*-dependent Pos(S) and Pos(LB) in NL 2DMs by Equation (2)[67,85]

$$\begin{aligned} &\mathrm{Pos}(S_{NN-i}) = \sqrt{2}\mathrm{Pos}(S_{21})\cos(i\pi/2N), \quad i = 1,2,\ldots,N-1 \\ &\mathrm{Pos}(LB_{NN-i}) = \sqrt{2}\mathrm{Pos}(LB_{21})\cos(i\pi/2N), \quad i = 1,2,\ldots,N-1 \end{aligned} \tag{2}$$

where $\mathrm{Pos}(S_{21})$ and $\mathrm{Pos}(LB_{21})$ are the S and LB frequency of 2L 2DM flakes. Because $\mathrm{Pos}(S_{\mathrm{bulk}}) = \sqrt{2}\mathrm{Pos}(S_{21})$ and $\mathrm{Pos}(LB_{\mathrm{bulk}}) = \sqrt{2}\mathrm{Pos}(LB_{21})$, $\mathrm{Pos}(S_{21})$ or $\mathrm{Pos}(LB_{21})$ in the Equation (2) can be obtained from $\mathrm{Pos}(S_{\mathrm{bulk}})$ or $\mathrm{Pos}(LB_{\mathrm{bulk}})$, respectively, once they can be measured in bulk LMs. Equation (2) can be used to deduce all the S or LB modes of 2DMs for different *N*.[67] The symmetry of 2DMs determines whether the S and LB modes are Raman active.[115] The intensity of the S and LB modes is determined by their EPC. For example, only S_{N1} peaks is observed in an intrinsic AB-NLG at room temperature, due to the weak EPC or Raman inactivity of other S or LB modes.[67] **Figure 11**a1,a2 plots the Raman spectra for NLGs with increasing N. Figure 11b shows the fitted Pos(G) and Pos(S) as a function of $1/N$. Whereas Pos(G) remains ≈1581 cm^{-1}, with no significant change with *N*, Pos(S) increases from 2LG to bulk graphite. Equation (2) describes all the experimental data. The only unknown parameter in Equation (2) is the interlayer coupling strength. By fitting the experimental data we can directly measure it. This result indicates that the interlayer coupling strength is constant in NLGs and independent on N. In Bernal-stacked MLG, the hardening of the S mode is not due to a variation of interlayer coupling, but rather to an increase of the overall restoring force (surface layers are less bound than in the bulk) going from 2LG to bulk graphite.

In bulk MoS_2, the LB mode is Raman inactive and the S mode is Raman active, and thus, one ULF mode only observed in bulk MoS_2 is attributed to the S mode. However, both the S and LB modes are Raman active in 2L MX_2. The observed one with frequency of $\mathrm{Pos}(S_{\mathrm{bulk}})/\sqrt{2}$ is attributed to the S mode and the other is the LB mode. **Figure 12**a shows experimental spectra of S and LB phonon branches of 1-10L and bulk MoS_2. Figure 12b,c show their experimental (squares) and LCM-based theoretical (crosses) frequencies of S and LB modes, respectively. The S modes observed experimentally are attributed to the $i = N$–1, $i = N$–3, and $i = N$–5 phonon branches, while the LB modes to the $i = 1$, $i = 3$, and $i = 5$ phonon branches in Equation (2). It shows that when $N > 6$, the frequency of the

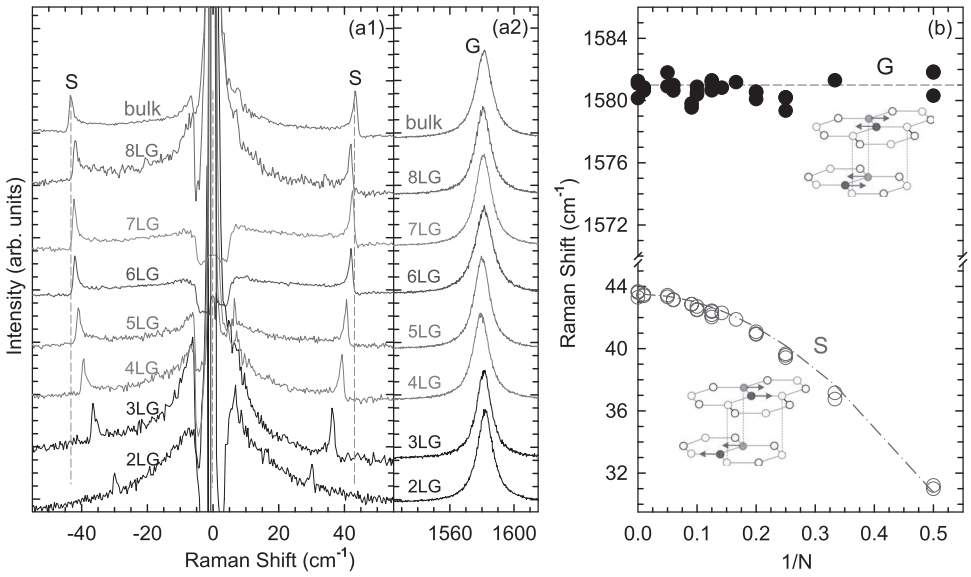

Figure 11. a1) Stokes/anti-Stokes Raman spectra for the S peak spectral region and a2) Stokes Raman spectra for the G peak spectral region. b) Pos(G) (filled black circles) and Pos(S) (open circles), as a function of 1/N. The blue dash-dotted line is a plot of Equation (2). Vertical dashed lines in (a1) and the horizontal line in (b) are guides to the eye. Adapted with permission.[67] Copyright 2012, Nature Publishing Group.

S modes with $i = N$-1 and the LB modes with $i = 1$ is weakly dependent on N. However, the frequency of other phonon branches of the S modes (*e.g.*, $i = N$-3 and $i = N$-5) and the LB modes (*e.g.*, $i = 3$ and $i = 5$) is still sensitive to N.

Graphite and MX_2 have a high symmetry (D_{6h}) The properties of these LMs are isotropic within the ab plane because of D_{6h} symmetry. The S modes of 2DMs corresponding to these LMs are degenerate. However, in an anisotropic multilayer 2DMs, such as NL BP and NL ReS_2, the S modes are nondegenerate and each pair of the S modes should be denoted as S_x and S_y. The LCM can also be applied to the nondegenerate S modes, and the frequencies of the $S^x_{N,N-j}$ and $S^y_{N,N-j}$ modes ($j = 1,2,...,N-1$) can also be expressed by Equation (2). Indeed, in NL ReS_2, two sets of the S modes are observed in 2-8L ReS_2

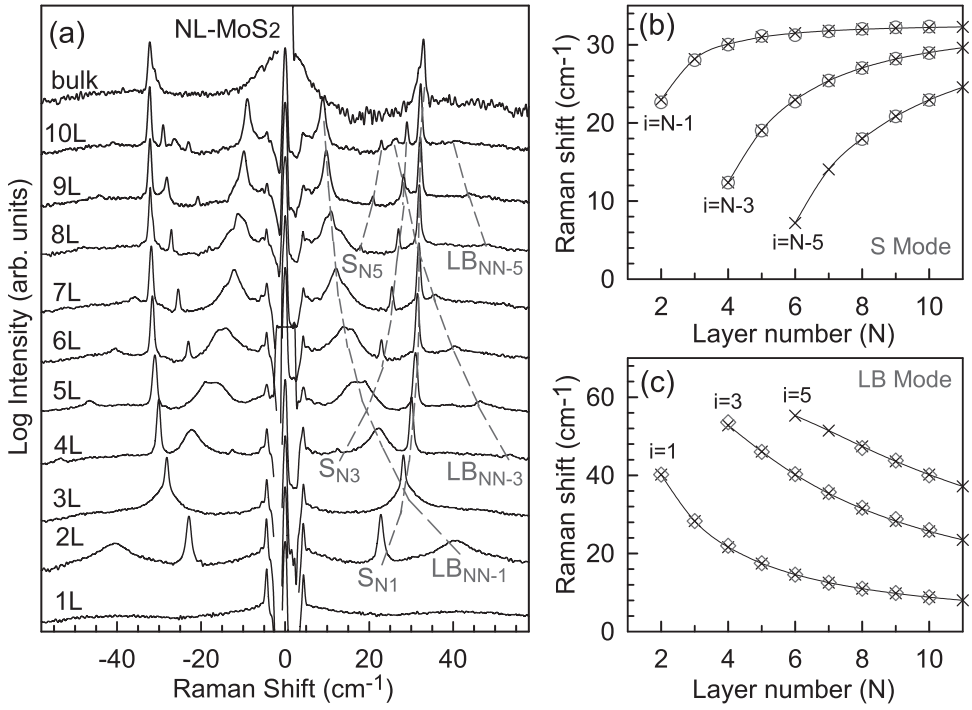

Figure 12. a) ULF Raman spectra of 1-10L and bulk MoS_2. The theoretical (crosses) and experimental (squares) frequencies of b) S and c) LB modes of 1-10L MoS_2. Adapted with permission.[85] Copyright 2013, APS.

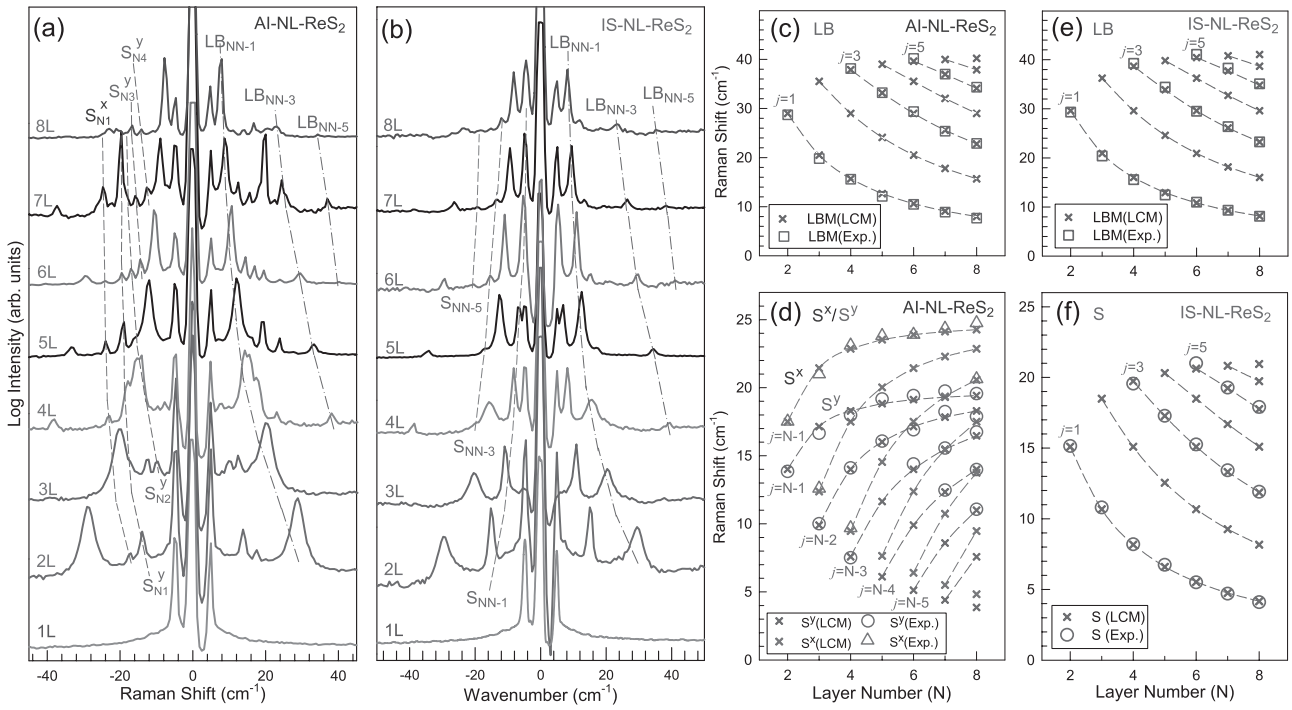

Figure 13. Low-frequency Raman spectra of 1-8L ReS_2 with a) AI-stacking and b) IS-stacking orders. The theoretical (crosses) and experimental (squares, circles, and triangles) frequencies of c) LB mode and d) C mode with AI-stacking order and e) LB mode and f) C mode with IS-stacking order in 2-8L ReS_2. Reproduced with permission.[47] Copyright 2016, Royal Society of Chemistry.

along with the LB modes, as shown in **Figure 13**a.[47] Similar to the case of NL MoS_2, the LB modes can be attributed to the $j = 1$, $j = 3$, and $j = 5$ phonon branches and decrease in frequency with increasing N for each branch, while the S modes in NL ReS_2 can be attributed to the $j = N–1$, $j = N–3$, and $j = N–5$ phonon branches and increase in frequency with increasing N for each branch, as depicted in Figure 13b,c. This stacking order is most stable and anisotropic in NL ReS_2 according to the theoretical simulation and is denoted as AI-stacking order and the corresponding NL ReS_2 as AI-NL-ReS_2. However, only one S mode is observed in 2L ReS_2 with another stacking order (see Figure 13d), which suggests that such stacking order is isotropic.[47] Its frequency lies between S^x_{21} and S^y_{21} of AI-2L-ReS_2. The isotropic-like stacked NL ReS_2 are denoted as IS-NL-ReS_2. However, the N-dependent Pos(S) in IS-NL-ReS_2 is quite different from that in AI-NL-ReS_2. Similar to the case of the LB mode, the S modes in IS-NL-ReS_2 can be attributed to the $j = 1$, $j = 3$ and $j = 5$ phonon branches and decrease in frequency with increasing N for each branch, as depicted in Figure 13e,f. The observed different branches of the S modes in AI- and IS-stacking orders result from the different symmetries and electron-phonon couplings between the two stacking orders.[47]

The S and LB vibrations are an intrinsic property of multilayer 2DMs, which are irrelevant to any substrate. Indeed, substrate effect can be ignored on Pos(S) and Pos(LB) of 2DM flakes. Because Pos(S) and Pos(LB) are linked with N by a robust general formula of Equation (2) based on LCM, therefore, the S and LB modes can be utilized to identify N of NL 2DM flakes and this method proves to be substrate-free. In principle, this technique can be applied to any 2DMs produced by micro-mechanical exfoliations, CVD growth, or transfer processes on various substrates, without the need for monolayer thickness and complex refractive index of 2DMs and the supporting substrate. The recent advance in ULF measurement techniques will make this N-identification method as a robust, fast, nondestructive and substrate-free approach for layer-number identification of ultrathin 2DM flakes.

The N-identification of NL 2DM flakes by ULF Raman modes can be also applied to 2D alloys, which can be alloyed by any of two or more 2DMs with similar properties. Here, we take $Mo_{0.5}W_{0.5}S_2$ alloys (simply denoted as $MoWS_2$ alloy) as an example to show how to identify N of $MoWS_2$ alloy flakes directly by the S mode of bulk alloy. In comparison to NL WS_2 and NL MoS_2, the E^1_{2g} and A_{1g} modes in $MoWS_2$ alloy exhibit broadened profiles due to the disorder effect. However, such disorder effect is generally absent for the interlayer vibrations of the $MoWS_2$ alloy,[19] as shown in **Figure 14**a. The S mode is Raman active in bulk alloy. Once $Pos(S_{bulk})$ is measured, one can obtain N-dependent peak positions of S^+_2 ($j = N–1$) and S^+_6 ($j = N–3$) branches via Equation (2) by $Pos(S_{21}) = Pos(S_{bulk})/\sqrt{(2)}$, as depicted in Figure 14b, which can be used for N determination. 1L alloy can be identified by the absence of ULF modes. Both the S and LB modes are Raman active in 2L $MoWS_2$ alloy, two ULF Raman modes can be observed in 2L alloy (Figure 14c). The S mode is located at $Pos(S_{bulk})/\sqrt{(2)}$ and the other mode is the LB mode with measured $Pos(LB_{21})$. The S and LB modes can be distinguished by the parallel (VV) and cross (HV) polarization configurations. The N-dependent peak positions of LB^-_2 ($j = 1$) and LB^-_6 ($j = 3$) branches (Figure 14d) via Figure (2) by $Pos(LB_{21})$ can be used to further confirm the N determination by the S^+_2 and S^+_6 branches. The N-dependent frequencies of both the S and LB modes are given in Figure 14e,f. Indeed, by

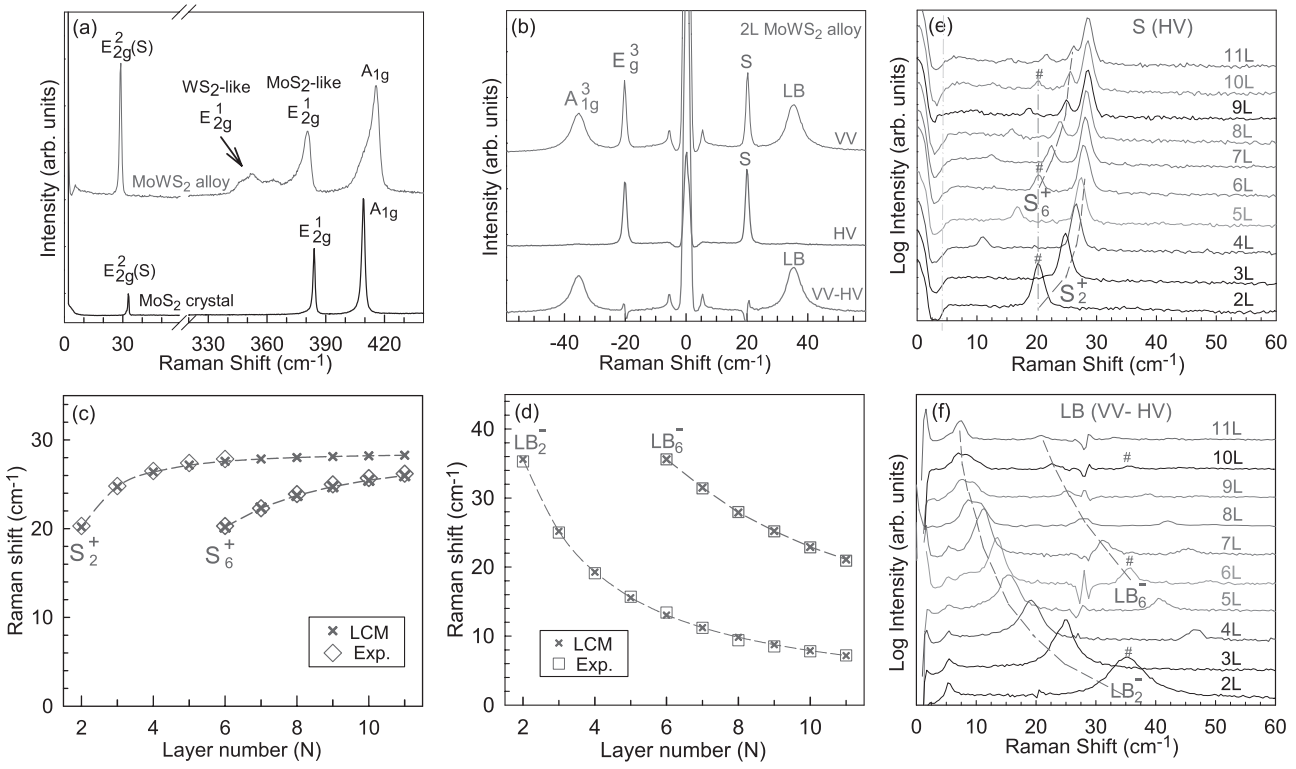

Figure 14. a) Raman spectrum of bulk $Mo_{0.5}W_{0.5}S_2$ alloy in 320–450 cm^{-1} ranges. b) Low-frequency Raman spectra of 2L $Mo_{0.5}W_{0.5}S_2$. The C mode is observable under both VV and HV configuration, while the LB mode is observable only under the VV configuration. Raman spectra of c) C phonon branches under the HV configuration and d) LB phonon branches under the VV-HV configuration in 2-11L $Mo_{0.5}W_{0.5}S_2$. The theoretical (crosses) and experimental (squares) frequencies of e) C and f) LB modes in 2-11L $Mo_{0.5}W_{0.5}S_2$. Adapted with permission.[19] Copyright 2015, AIP.

comparing the experimental and theoretical peak positions of the S modes of the S^+_2 and S^+_6 branches and the LB modes of LB^-_2 and LB^-_6 branches, the N of $MoWS_2$ alloy flakes can be determined. Therefore, once the S and (or) LB modes of bulk $MoWS_2$ alloy can be measured, whose frequencies can be used to identify $MoWS_2$ alloy flakes even though the supporting substrate and alloy composition are unknown.

4.3. Davydov Splitting

The frequency of HF modes in NL MX_2 flakes should be dependent on the interlayer coupling between adjacent layers, i.e., the coupling between two nearest X atoms in adjacent layers if only the nearest coupling is considered.[57] Once the nearest X atoms in adjacent layers vibrate out of phase, the additional vdW interaction between the nearest X atoms in adjacent layers will raise the frequency of the Raman mode with respect to the mode whose nearest X atoms in adjacent layers vibrate in phase, leading to Davydov splitting.[57] Considering that two identical coupled entities have vibrational frequencies given by ω_0 and ω_c, where ω_0 is the frequency of the isolated entity and that of two uncoupled entities when the two entities vibrate in phase, and ω_c is the frequency of two coupled entities in which they vibrate out of phase, if $\Delta\omega$ is the coupling frequency between two coupled entities, the three frequencies have the relation of $\omega_c^2 = \omega_0^2 + \Delta\Omega^2$.[116] 2L MX_2 can exhibit clear signature of the Davydov splitting as the case the S modes in twisted (2+2)LG.[42,117] However, only one of the two Davydov components is usually Raman active, and it is difficult to directly observe Davydov splitting in 2L MX_2.

We take the A'_1 mode in 1L $MoTe_2$ as an example to discuss how the LB vibrations significantly affect the frequency of the HF A'_1-like modes in multilayer $MoTe_2$. The A'_1 mode in 1L $MoTe_2$ will split into N A'_1-like modes in NL $MoTe_2$ ($N > 1$). These modes can be expressed as $\frac{N+1}{2}A'_1 + \frac{N-1}{2}A''_2$ for ONL $MoTe_2$ and $\frac{N}{2}A_{2u} + \frac{N}{2}A^2_{1g}$ for ENL $MoTe_2$,[10,57,93] where the A'_1 and A^2_{1g} modes are Raman active and the A''_2 and A_{2u} modes are infrared active. Therefore, for ONL $MoTe_2$, it is expected to observe (N+1)/2 Davydov components of A'_1-like mode, and N/2 Davydov components of A'_1 mode would be observed in ENL $MoTe_2$ in the corresponding Raman spectra. For the A'_1-like modes NL $MoTe_2$, the observed Raman spectra are usually the Davydov component with the highest frequency, while the frequency of the uncoupled Davydov component should be the lowest one among the N Davydov components, which is equal to that of the A'_1 mode of 1L $MoTe_2$ if only the nearest interlayer coupling is considered. Indeed, N Raman-active A'_1-like Davydov components have been clearly observed in both the (2N-1)L and 2NL $MoTe_2$ flakes ($N > 1$), as shown in **Figure 15**a.[57] Davydov splitting has also been observed in the WS_2, MoS_2, and $MoSe_2$.[58,97,118]

The S and LB modes are the direct signatures of interlayer coupling in 2DMs, and the Raman spectra of the S and LB modes in NL $MoTe_2$ flakes are shown in Figure 15b. Because the atomic displacements of the A'_1-like modes are perpendicular to

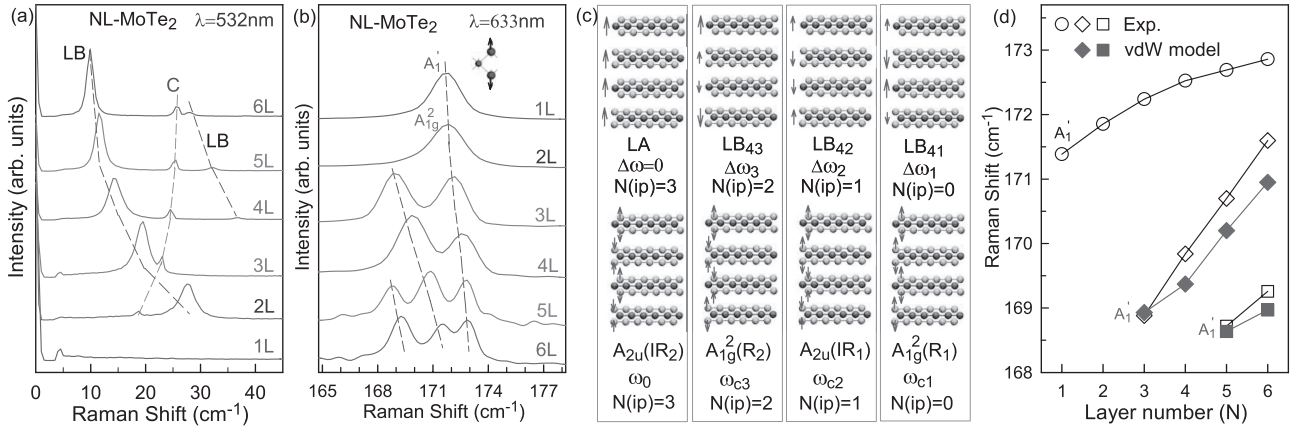

Figure 15. a) The Raman spectra of 1-6L $MoTe_2$ flakes in the ULF region by 532 nm. b) The A'_1 ($A^2{}_{1g}$) modes in 1-6L $MoTe_2$ excited by 633 nm. Raman spectra are normalized to the strongest peak and are offset for clarity. c) Schematic diagram of the vdW model for Davydov splitting in 4L $MoTe_2$. N(ip) is the number of the in phase vibration interface. d) The calculated frequency (solid diamonds and squares) of each Davydov component of the A'_1-like modes in 3-6L $MoTe_2$ based on the experimental (Exp.) value (gray solid circles) of the Davydov component with highest frequency and the vdW model, and the corresponding experimental (open diamonds and squares) frequency of each Davydov component of the A'_1-like modes. The experimental frequency of the A'_1-like modes in 1-2L $MoTe_2$ is also included. Adapted with permission.[57] Copyright 2016, APS.

the basal plane, the interlayer LB coupling can be closely related to the frequency difference between Davydov components. We take the 4L $MoTe_2$ as an example, the atomic displacement of the A'_1-like and LB modes are plotted in Figure 15c. The A'_1-like and LB modes with the same number of the in phase vibration interface (N(ip)) are plotted together. If only the nearest interlayer coupling, the frequency of the LB modes are the coupling frequency ($\Delta\omega_i$, i = 1,2,3) of Davydov components in 4L $MoTe_2$. The A_{2u} (IR_2) mode is the uncoupled entities with a frequency of ω_0, and the other three modes are the coupled entities with the frequencies of ω_{ci}, i = 1, 2, 3, respectively. The frequencies ω_0, ω_{ci} and $\Delta\omega_i$ will satisfy the vdW model of $\omega_{ci}^2 - \Delta\omega_i^2 = \omega_0^2$ (i = 1,2,3). Based on the vdW model and the observed Davydov component with the highest frequency, the calculated frequency of other Davydov components in 3-6L $MoTe_2$ are depicted in Figure 15d by solid diamonds and squares, which is in good agreement with the experimental data. It is found that the difference in the electron-phonon coupling strength between two Davydov components may result in different resonant profiles, and thus proper excitation energy must be chosen to observe the Davydov splitting in NL $MoTe_2$ ($N > 2$).

In principle, the frequency of uncoupled entities in NL $MoTe_2$ should be equal to that of the isolated entity because all the nearest Te atoms in adjacent layers vibrate in phase. Therefore, Pos($A'_1(R_2)$) in 3L $MoTe_2$ should be the same as Pos(A'_1) in 1L $MoTe_2$. However, the frequency difference between the A'_1 mode in 1L $MoTe_2$ and the $A'_1(R_2)$ mode in 3L $MoTe_2$ is about 2.5 cm^{-1}. Even so, the Davydov splitting between $A'_1(R_1)$ and $A'_1(R_2)$ in 3L $MoTe_2$ can be well understood by the vdW model. This suggests that the Davydov splitting in 3L $MoTe_2$ is mainly determined by the interlayer vdW interactions, which provides a direct evidence from Raman spectroscopy of how the nearest vdW interactions significantly affect the frequency of HF modes in multilayer $MoTe_2$. The above vdW model can be also extended to the Davydov splitting of HF modes associated with the S modes and to the Davydov splitting in other 2DM flakes. This presents a simple way to identify N of ultrathin $MoTe_2$ flakes by the corresponding number and peak position of Davydov components.

4.4. N-Dependent Si Mode Intensity from SiO_2/Si Substrate

The intensity of the Si mode from SiO_2/Si substrate underneath 2DM flakes (I_{2dm}(Si)) is significantly dependent on N and usually decreases monotonically with increasing N of 2DM flakes, since 2DM flakes on SiO_2/Si substrate can absorb both laser beam reflected from Si substrate and Raman signal from Si substrate to some extent. This absorption is hardly modified by the small amount of defects and disorders in 2DM flakes.[119–121] Taking NLGs on SiO_2/Si substrate (h_{SiO_2} = 89 nm) as an example, the intensity of the Si mode from SiO_2/Si substrate underneath NLG flakes is denoted as I_{2dm}(Si) and that from the bare SiO_2/Si substrate is denoted as I_0(Si). Schematic diagram of Raman measurements to measure the ratio of $I_{2dm}(Si)/I_0(Si)$ is demonstrated in **Figure 16**a. The measured $I_{2dm}(Si)/I_0(Si)$ with NA = 0.45 and excitation of 532 and 633 nm are plotted in Figure 16b. N-dependent $I_{2dm}(Si)/I_0(Si)$ can be well understood by the multiple reflection interference model,[72] as shown in Figure 16b. It shows that different excitation wavelengths give different trends for N-dependent $I_{2dm}(Si)/I_0(Si)$. However, for both the excitation wavelengths, $I_{2dm}(Si)/I_0(Si)$ decreases monotonically with increasing N of NLG flakes.

Because the Raman intensities of HF modes in 2DMs flakes and the Si mode are very sensitive to both the crystal orientation of 2DM flakes and Si substrates and to the laser polarization, the N identification by the ratio between Raman intensities of HF mode in 2DMs flakes and Si mode cannot be used as a standard method for general application. However, I_{2dm}(Si) and I_0(Si) are from the same Si substrate, so it does not need to consider crystal orientation of Si substrate. Therefore, we can identify N of intrinsic and defective NLG flakes up to N = 100 by comparing the theoretical and experimental ratios of

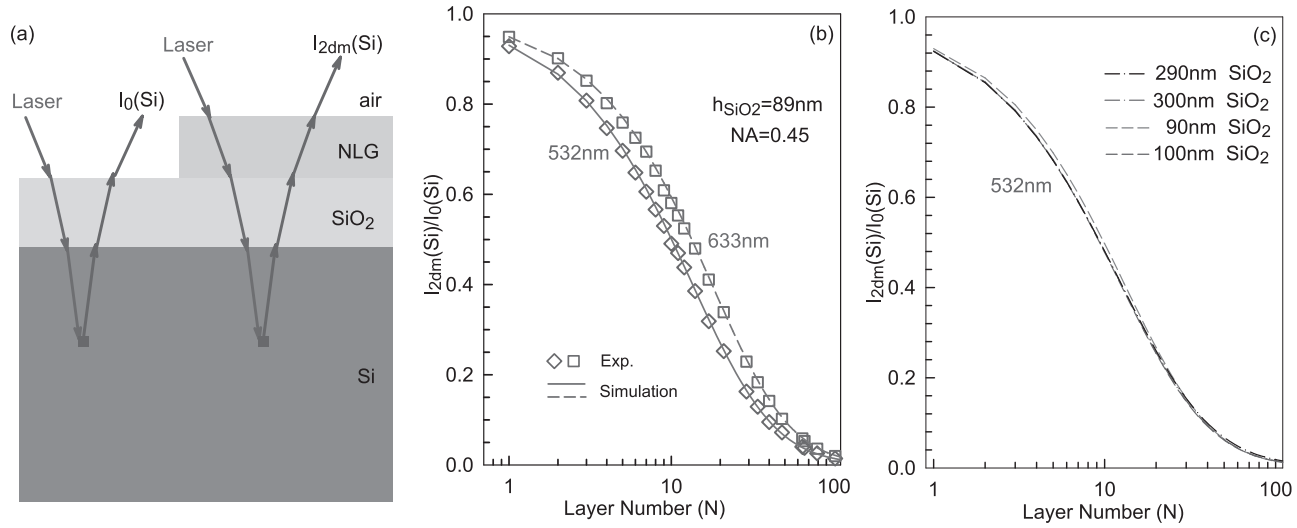

Figure 16. a) Schematic diagram of Raman measurements of $I_{2dm}(Si)/I_0(Si)$. b) The theoretical curves (solid and dashed lines) and experimental data (diamonds and squares) of N-dependent $I_{2dm}(Si)/I_0(Si)$ for 532 nm and 633 nm excitations, NA = 0.45. c) The calculated N-dependent $I_{2dm}(Si)/I_0(Si)$ excited by a 532 nm excitation for different h_{SiO_2}. NA = 0.45. Adapted with permission.[72] Copyright 2015, Royal Society of Chemistry.

$I_{2dm}(Si)/I_0(Si)$.[72] During the measurement, one can rotate the Si substrate to get a maximum intensity of the Si mode from bare SiO_2/Si substrate to reach a high signal-to-noise of $I_{2dm}(Si)/I_0(Si)$. h_{SiO_2} is an important parameter to determine $I_{2dm}(Si)/I_0(Si)$, however, $I_{2dm}(Si)/I_0(Si)$ for NLG flakes on substrate with h_{SiO_2} = 290, 300, 90, and 100 nm at 532 nm excitation are almost identical to each other, as shown in Figure 16b, suggesting 532 nm excitation is a good choice to identify N of NLG flakes by $I_{2dm}(Si)/I_0(Si)$. The monotonically trend and high signal-to-noise make $I_{2dm}(Si)/I_0(Si)$ identify N of NLG flakes on SiO_2/Si substrate with small error. The N deviation given by 532 or 633 nm excitations is very small, almost zero for $N \leq 15$, less than 1 for $16 \leq N \leq 40$, and less than 3 for $41 \leq N \leq 100$.

There are several advantages of the N identification based on $I_{2dm}(Si)/I_0(Si)$: (1) The Raman intensity from Si substrates is usually so intense that the signal-to-noise of the measured $I_{2dm}(Si)/I_0(Si)$ can be very high. (2) In contrast to $I(G)/I_0(Si)$ or $I(G)/I_{2dm}(Si)$, this technique does not need to introduce an undetermined Raman efficiency of different atoms in the intensity calculation for the corresponding Raman modes. (3) Because the Si peaks is from the same Si substrate, it makes the measured value of $I_{2dm}(Si)/I_0(Si)$ robust for any substrate orientation and laser polarization. (4) $I_{2dm}(Si)/I_0(Si)$ is not affected by slight disorders molecule adsorption and doping if they do not significantly modify $\tilde{n}_\lambda$ of 2DMs. (5) The N identification based on Raman spectroscopy offers a high spatial resolution for other optical techniques, such as OC.

$I_{2dm}(Si)/I_0(Si)$ is also sensitive to N of other 2DM flakes, such as ultrathin MX_2 flakes. Because the used NA, h_{SiO_2} and laser wavelength may be different in different laboratory, one must compare the experimental $I_{2dm}(Si)/I_0(Si)$ with theoretical one to precisely identify N of NL MX_2 deposited on the SiO_2/Si substrates. However, due to the lake of a unified $\tilde{n}$ for NL MX_2 from 1L to multilayer, it is difficult to calculate $I_{2dm}(Si)/I_0(Si)$ by the multiple reflection interference model. To obtain a unified $\tilde{n}_{eff}$ for NL MX_2 from 1L to multilayer, we assumed the real part of $\tilde{n}_{eff}$ of NL MX_2 as that of 1L MX_2 and treated the imaginary part of $\tilde{n}_{eff}$ as a fitting parameter to fit the experimental intensity ratio of $I_{2dm}(Si)/I_0(Si)$ for each laser excitation. $\tilde{n}_{eff}$ of MoS_2, WS_2, and WSe_2 are obtained for typical laser excitations (488 and 532 nm) and can be used to well fit N-dependent $I_{2dm}(Si)/I_0(Si)$ for SiO_2/Si substrates with $h_{SiO_2} \simeq 90$ nm, as shown in **Figure 17**.[86] The fitted $\tilde{n}_{eff}$ of MoS_2 has been used to identify N of MoS_2 flakes deposited on SiO_2/Si substrates with h_{SiO_2} = 302 nm, which agrees well with that determined from their S and LB modes.[86] This provides a way to identify N of 2DM flakes with N-dependent $\tilde{n}$ by measuring Raman intensity from substrate.

For application purposes of N identification of TMD and MLG flakes for the research community, $I_{2dm}(Si)/I_0(Si)$ of TMD flakes deposited on SiO_2/Si substrate is provided in the supplementary data of Li et al.[86] for commonly used excitation energies (2.34 and 2.54 eV) and h_{SiO_2} of 80~110 nm and 280~310 nm, along with the corresponding data for MLG.

5. Optical Absorption

As discussed above, the N-dependent optical absorption is fundamental to understand OC of 2DM flakes and Raman intensity of 2DM flakes or substrates for N identification. For the suspended flakes or flakes laying on transparent substrate, the absorption spectra can be measured directly.[37,53,123–126]

The opacity of suspended graphene is defined solely by the fine structure constant, $a = e^2/\hbar c \approx 1/137$ (where $\hbar$ is reduced Planck's constant, e the electron charge and c is the speed of light), the parameter that describes coupling between light and relativistic electrons and that is traditionally associated with quantum electrodynamics rather than materials science.[37,124] Despite being only one atom thick, graphene is found to absorb a significant ($\pi a = 2.3\%$) fraction of incident white light, a consequence of graphene's unique electronic structure. The transmittance of 1LG is $T = (1 + 0.5\pi a)^{-2}$ and $R = 0.25\pi^2 a^2 T$. Because the structure constant is quite small, ≈1/137, the R can be neglected.

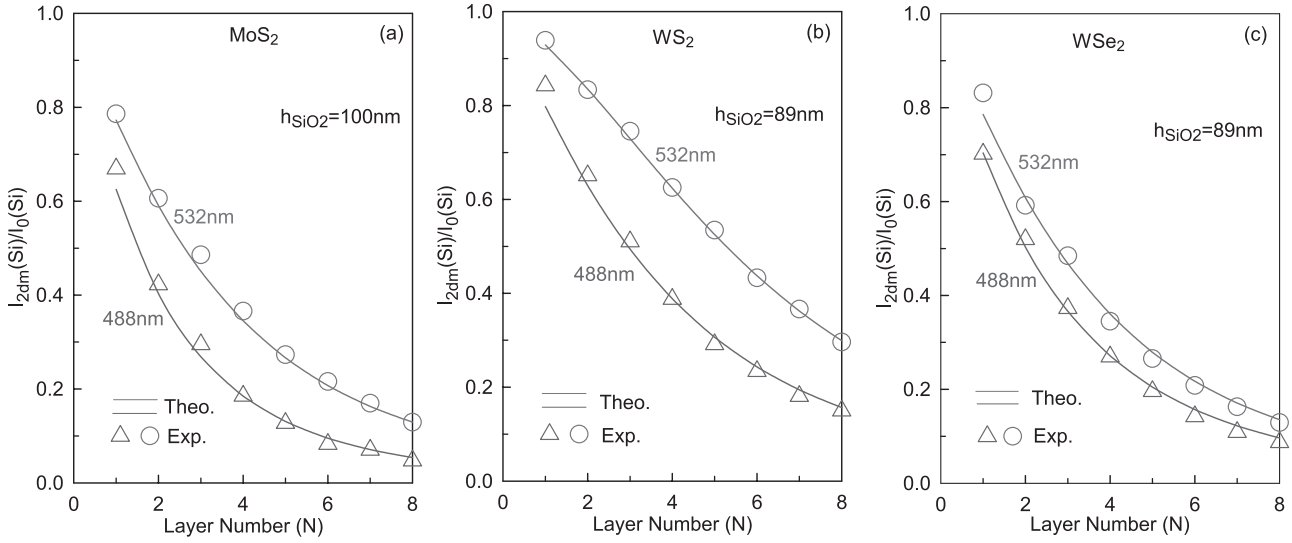

Figure 17. The theoretical curves and experimental data (triangles and squares) of $I_{2dm}(Si)/I_0(Si)$ of a) NL MoS_2, b) NL WS_2, and c) NL WSe_2 by 488 and 532 nm excitations. Adapted with permission.[86] Copyright 2016, IOP Science.

Thus, $(1-T) \approx \pi a$, and rption coefficient can be detected by the transmittance spectra, as shown in **Figure 18**a. Figure 18b shows the experimental and theoretical data of the transmittance spectra for 1LG. The absorption coefficient of 1LG is unified at the white light range. Moreover, the intensity of transmittance spectra reduce by πa with each added layer for 1–5 layers.

For ultrathin TMD flakes supported by a transparent substrate, differential reflectance provides an effective measure of absorbance.[53,69,125,126] The fractional change in reflectance δR for a thin layer sample relative to the reflectance of a dielectric substrate with refractive index of n_{subs} is related to the absorbance (A) of the material by: $\delta R(\lambda) = \frac{4}{n_{subs}^2 - 1} A(\lambda)$.[127] n_{subs} can be assumed as wavelength independent for the visible spectral range on the quartz substrate. All peaks exhibit a gradual but distinct blueshift with decreasing flake thickness.[53] N-dependent absorption can also be expected in other 2DMs, such as BP, ReS_2 and InSe.[128–130]

Because the absorbance of 2DM flakes usually increases with increasing N, the transmittance spectra (absorption spectra) can be used to identify the N of 2DM flakes, such as MLGs and TMDs. However, due to the measurement requirement of absorption spectra, it just is suitable to identify the N of 2DM flakes that are suspended or on transparent substrate.

6. Photoluminescence

Most MX_2 are indirect gap semiconductors in bulk, but transform to direct gap semiconductors when thickness is reduced to monolayer.[33,34,53] The indirect-to-direct transition is attributed to the absence of weak interlayer coupling in the monolayer,[33,34,131] which was directly verified in NL $MoSe_2$ via interlayer thermal expansion. An excited electron will attract a hole by Coulomb interactions to form a bound state (called an exciton) with the bound energy levels lying in the band-gap region. This excitonic effect is significantly enhanced in 2DMs owing to strong spatial confinement and a reduced screening effect.[132–135] Thus, as a 2DM, 1L MX_2 is expected to have a strong excitonic effect with a large exciton binding energy of 0.5–1.0 eV,[136–138] which will significantly influence its optical properties, e.g., PL and optical absorption.

The indirect-to-direct band-gap transition from bulk to 1L MoS_2 (also WS_2, WSe_2, and $MoSe_2$) leads to enhanced PL emission in 1L MoS_2 and decrease in PL intensity with increasing N. For 2-6L MoS_2 and some of other MX_2 flakes, the indirect band gap (lowest PL peak position) decreases with increasing N. **Figure 19**a,b show PL spectra of 1-6L MoS_2 and 1-6L WS_2, respectively. The PL spectrum of 1L MoS_2 and 1L WS_2 consists of a single narrow feature due to their direct band-gap structure, which make them be easily distinguished from their multilayer. In contrast, there are multiple emission peaks in 2-6L MoS_2 and 2-6L WS_2, where the lowest-energy peak (labeled as I) shifts to lower energies with increasing N due to the indirect band-gap structure changing with N. The transitions of NL MoS_2 and WS_2 with lowest energies are summarized in Figure 19c,d. Therefore, the lowest transition energy in PL spectra can be used to identify N of NL MoS_2 and NL WS_2 when $N < 6$. This technique can also be applied to other MX_2 flakes, such as WSe_2, $MoSe_2$ and $MoTe_2$.

The N-dependent PL spectra have also been measured from other semiconducting 2DM flakes, such as ReS_2, $ReSe_2$, and BP.[47,55,56,107] 1L ReS_2 and both AI- and IS-NL-ReS_2 are direct band-gap semiconductors. The PL profile of AI-NL-ReS_2 is similar to that of 1L ReS_2. However, the PL profile of IS-NL-ReS_2 is narrower and shows a sharper peak at the peak center. These different PL features can be adopted as a gauge to distinguish the IS-NL-ReS_2 from the AI stacked ones, while the peak position can be further used to identify N for ReS_2 flakes.[47] NL BP ($N \geq 1$) is also direct gap semiconductor. The band gap of NL BP varies from each other strongly from 1.5–2.0 eV in 1L BP to ~0.8 eV in 5L BP,[55,56] due to the strong interlayer coupling. Because of its instability, N of BP flakes cannot be reliably determined by their PL peaks.

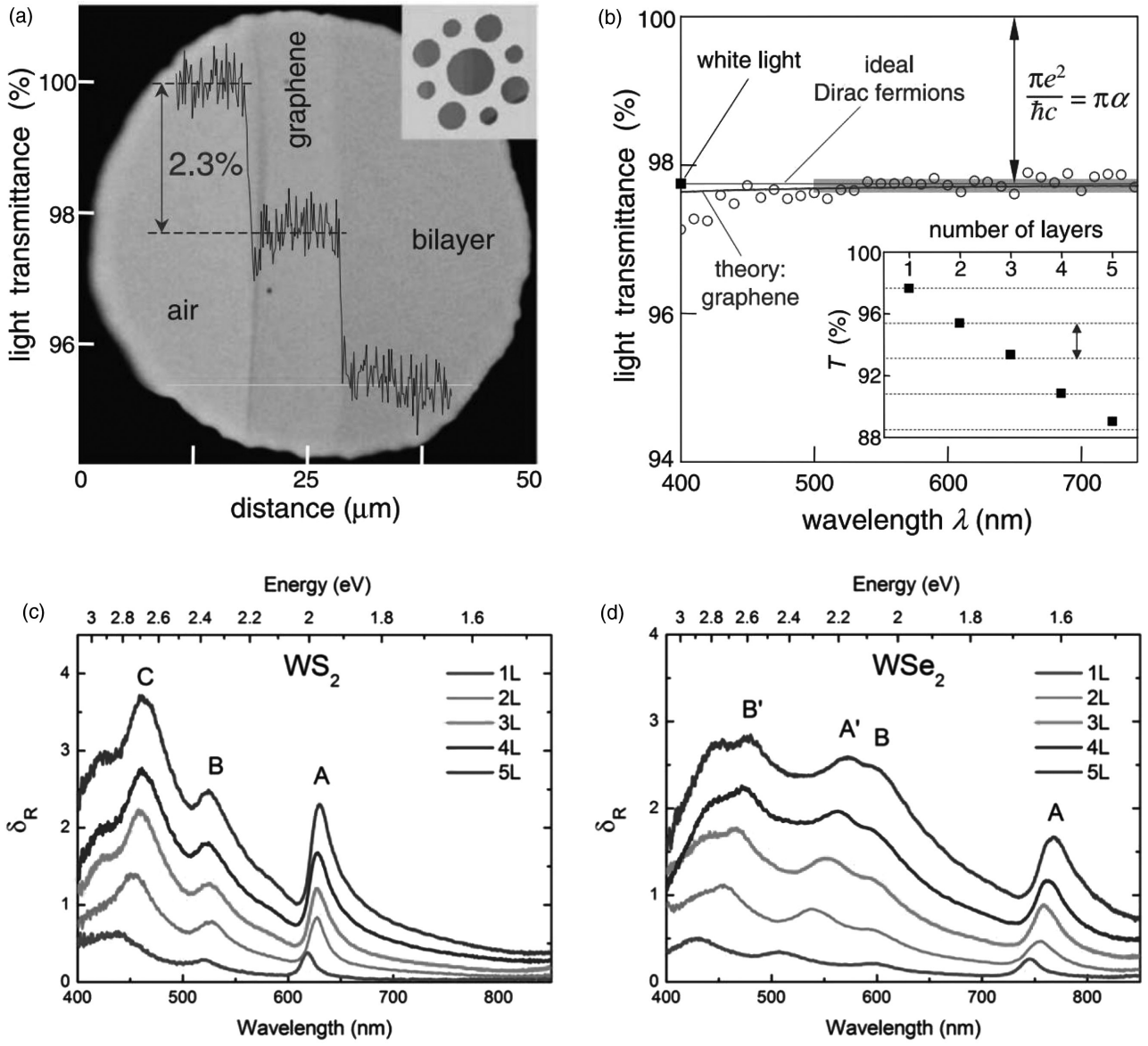

Figure 18. a) Photograph of a 50 μm aperture partially covered by 1LG and 2LG. The line scan profile shows the intensity of transmitted white light along the yellow line (Inset). The sample design: A 20 μm thick metal support structure has several apertures of 20, 30, and 50 μm in diameter with graphene crystallites placed over them. b) Transmittance spectrum of 1LG (open circles). The red line is the transmittance $T = (1 + 0.5\pi\alpha)^{-2}$ expected for 2D Dirac fermions, whereas the green curve takes into account a nonlinearity and triangular warping of graphene's electronic spectrum. The gray area indicates the standard error for the measurements. (Inset) Transmittance of white light as a function of the number of graphene layers (squares). The dashed lines correspond to an intensity reduction by $\pi\alpha$ with each added layer. (a,b) Reproduced with permission.[37] Copyright 2008, AAAS. Differential reflectance spectra of mechanically exfoliated c) 2H-WS_2 and d) 2H-WSe_2 flakes consisting of 1–5 layers. The peaks are labeled according to the convention proposed by Wilson and Yoffe.[122] Panels (c) and (d) reproduced with permission.[53] Copyright 2006, APS.

7. Second Harmonic Generation

The lack of an inversion center in the crystalline structure of the material (so that energy gaps at the K and K′ valleys with finite but opposite Berry curvatures are introduced) is an underlying reason for developing interesting properties. Actually, the inversion asymmetry of the material not only affects its electronic and linear optical properties but also gives rise to a finite second-order optical nonlinearity ($\chi(2) \neq 0$).[139] Thus, the SHG can be observed in 2DM flakes with noncentrosymmetric structure.

The monolayer and odd-layer of MX_2 and BN flakes do not have the inversion center, and the even-layer and bulk are with inversion center, as shown in **Figure 20**a. For a specific number of layers, the intensity of SHG depends on the crystal orientation, as shown in Figure 20b. The polarization behavior of SHG intensity in odd-layer MoS_2 and BN obey the $\cos^2(3\theta)$ law, i.e., $I_{\parallel} = I_0 \cos^2(3\theta)$, where θ is the angle between the mirror plane in the crystal structure and the polarization of the pump beam, I_0 is the maximum SHG intensity and $I_{\parallel}$ is the SHG intensity under parallel configuration, as shown in Figure 20b.

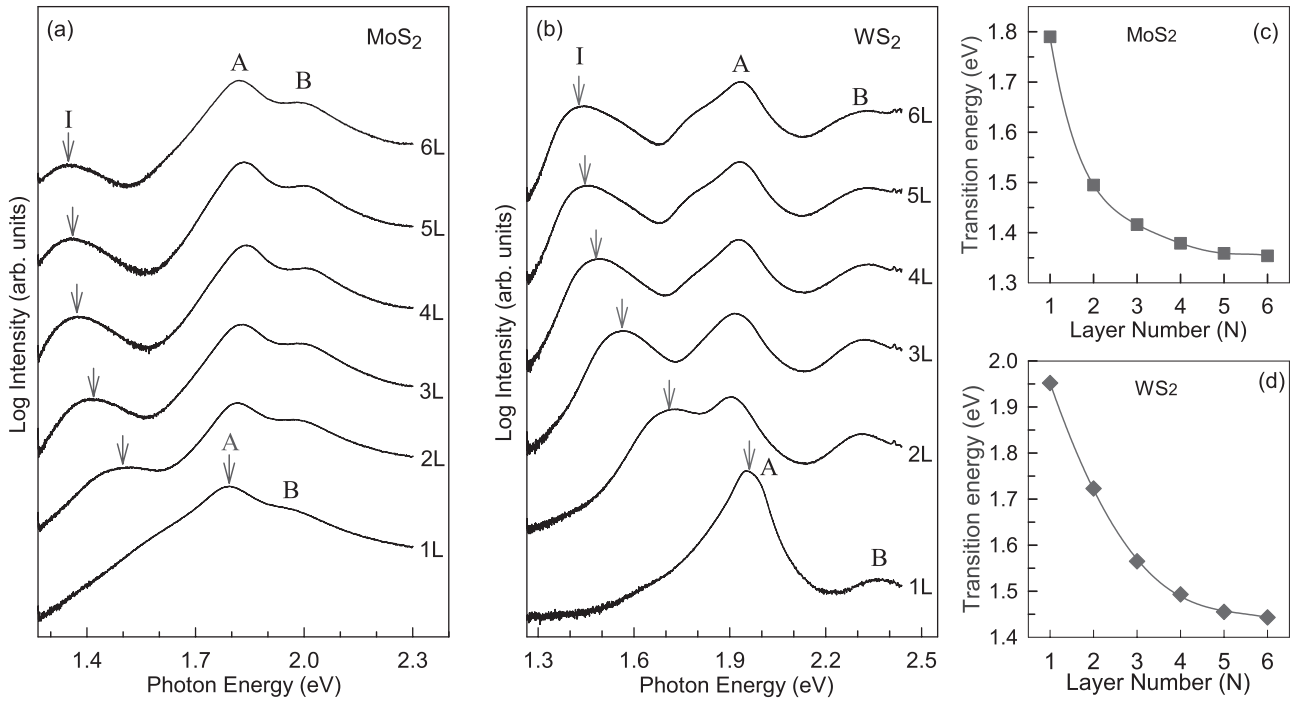

Figure 19. PL spectrum of a) 1-6L MoS_2 and b) 1-6L WS_2, where the lowest-energy peak is labeled by arrow. The lowest transition energies in c) NL MoS_2 and d) NL WS_2 as a function of *N*.

It's because of the six-fold symmetry in MoS_2 and BN. Moreover, the SHG intensities in MoS_2 and BN are dependent on *N*, and can be understand by the wave propagation effects. In the 2H-MoS_2 and AB-stacked BN, the sign of the SH susceptibility in adjacent layers is alternating. Thus, for flakes with odd N, the signals from adjacent layers would cancel each other, leading to a very weak and undetectable SHG response. For flakes with odd *N*, in the simplest picture, the signal from a block of N-1 layers fully cancels out, leaving the residual signal from just one layer. Thus, no thickness dependence would be

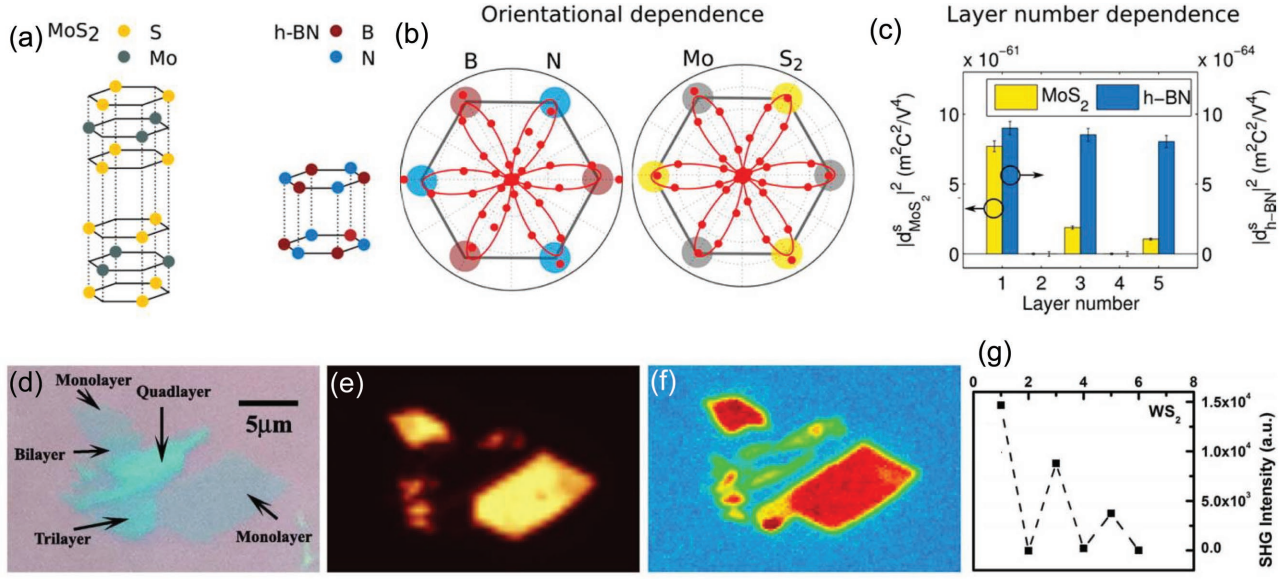

Figure 20. a) Structures of repeating two-layer units in 2H-stacked MoS_2 and h-BN. b) Polar plots of the SHG intensity from 1L BN and 1L MoS_2 as a function of the crystal's azimuthal angle θ. c) N-dependent SHG intensities for 1-5L MoS_2 and 1-5L h-BN. (a–c) Reproduced with permission.[69] Copyright 2013, American Chemical Society. d) Optical images of WS_2 flakes on SiO_2/Si substrates with h_{SiO_2} = 300 nm. e) PL images at direct gap transition energy of the corresponding WS_2 flakes excited at 2.41 eV. Only 1L WS_2 are visible at the present contrast. f) The corresponding SHG under an 800 nm excitation at normal incidence (150 fs, 80 MHZ) on WS_2 flakes. The highest intensity labeled in red arises from 1L WS_2. g) N-dependent SHG intensity in WS_2 flakes, showing an even-odd oscillation. (d–g) Reproduced with permission.[71] Copyright 2013, Nature Publishing Group.

expected. However, the interlayer coupling and optical absorption should be considered here. The photon energy of SHG (3.1 eV) is higher than the band gap of MoS_2. Thus, the SHG photon would be absorbed by MoS_2. The increased absorption from 1L to 5L MoS_2 leads to the decreased SHG intensity with respect to N as shown in Figure 20c.[69] For BN flakes, due to the photon energy of SHG (3.1 eV) is lower than the band gap, the effect of the optical absorption can be neglected, and the SHG intensity just slightly decreases with *N*, as shown in Figure 20c. The similar behaviors can be observed in WS_2 flakes, as shown in Figure 20d–g.[71] Therefore, in the ONL MX_2, like MoS_2 and WS_2, the SHG intensity decreases with increasing *N*, which makes the SHG intensity can used to identify N of ONL MX_2.

Among the recent advances, 2D gallium selenide (GaSe), a layered III-VI semiconductor, has been receiving lifted attention from electronic and optoelectronic applications.[140] Because of the existence of the inversion center, there is no SHG signal from 1L GaSe. There are several different modifications which differ in the stacking sequence, and the three most important classifications are so-called β-GaSe, ε-GaSe, and γ-GaSe.[141] β-GaSe has two basic layers per unit cell and belongs to the space group D^4_{6h} with an inversion symmetric center. On the other hand, the layered structure of ε-GaSe is generated from one primitive layer by translations. ε-GaSe is thus noncentrosymmetric and belongs to the space group D^1_{3h}. Therefore, the SHG signal can be detected from the multilayer ε-GaSe, but not from β-GaSe. Fortunately, the main stacking order in bulk materials is ε-GaSe.[70] In the multilayer GaSe produced by mechanical exfoliation method, the SHG can be observed. Moreover, because the symmetry of GaSe is different from the MX_2, the interlayer cancel effect of the SHG signal would not happen in GaSe, and the SHG intensity in GaSe increase with increasing *N*. The SHG signal of multilayer GaSe above 5L shows a quadratic dependence on *N*, while that of a flake thinner than 5L shows a cubic dependence. The discrepancy between the two SHG responses is attributed to the weakened stability of noncentrosymmetric ε-GaSe in the atomically thin flakes where a layer-layer stacking order tends to favor centrosymmetric modification, i.e., β-GaSe.[70]

N-dependent SHG intensity can be employed to determine N of 2DM flakes with noncentrosymmetric structure. As discussed above, the SHG intensity depend on the crystal orientation when there is an analyzer in front of the detector for the linear polarized laser.[142,143] Thus, before comparing the relative intensities of 2DM flakes with different N, one should make sure that all the signals are measured without the analyzer or under an circular polarized or nonpolarized laser. The resonance between the SHG pump photon and optical absorption peak can enhance the intensity strongly, so the energy of the pump laser should be chosen carefully to be out of the resonant window.[144,145]

8. Conclusions

The neighboring layers of layered LMs can easily slide against each other so that a single monolayer or multilayer can be fabricated by mechanical exfoliation to form atomically thin crystals, known as 2DMs. The properties of 2DMs are highly related to their *N*. Here, we review the evolution of optical properties (*e.g.*, OC, Rayleigh scattering, Raman spectroscopy, optical absorption, PL and SHG) of several typical 2DMs from monolayer to multilayer when they are suspended or deposited on some kinds of substrates. The optical parameters of peak position, peak area (intensity) and linewidth are discussed in detail to reveal how to utilize these optical parameters to rapidly and accurately determine N or thickness of the 2DM flakes in their own applicable scope, which is essential to their fundamental studies and practical applications. These optical techniques also have own disadvantages in terms of determining *N* of 2DM flakes and may cause ambiguity for providing reliable information if they are not utilized properly. In this case, for some specific 2DM flakes, the combination of two or more optical techniques are necessary to accurately determine their N or thickness.

There are now reported to be several hundred companies worldwide producing or using graphene and other 2DMs. Many issues must be concerned to face the large-scale production, processing and application of 2DMs when one consider the world outside of the laboratory. For industry to have confidence in graphene materials produced commercially, the properties of these materials must be accurately, reliably and reproducibly measured. The properties of 2DMs are highly related to their thickness, *i.e.*, layer number (*N*), and thus the *N* determination of 2DM flakes is critical to cater to quality appraisals for the 2DM industrial products. Therefore, standardization on the N determination of 2DM flakes will be crucial to allow the comparison of flake thickness for many different 2DMs produced worldwide, as well as for comparisons against different technologies. This review demonstrates that these optical techniques can be expected to service as robust, fast, accurate, nondestructive and even substrate-free approaches for *N* counting or thickness identification of 2DM flakes produced by micromechanical exfoliations, CVD growth, or transfer processes on various substrates, which bridges the gap between the characterization and international standardization for thickness determination of 2DM flakes and the gap between academia and industry.

Acknowledgements

X.-L.L., W.-P.H., and J.-B.W. contributed equally to this work. The authors acknowledge support from National Basic Research Program of China (Grant No. 2016YFA0301200), National Natural Science Foundation of China (Grant Nos. 11225421, 11434010, 11474277, 11504077, 11574305, 51527901, 11604173), Natural Science Foundation of Shandong Province in China (Grant No. BS2015CL013), Program of Science and Technology in Qingdao City (Grant No. 15-9-1-112-jch) and National Young 1000 Talent Plan of China.

Received: August 29, 2016
Revised: October 24, 2016
Published online:

[1] K. Novoselov, D. Jiang, F. Schedin, T. Booth, V. Khotkevich, S. Morozov, A. Geim, *Proc. Natl. Acad. Sci. USA* **2005**, *102*, 10451.

[2] J. N. Coleman, M. Lotya, A. O'Neill, S. D. Bergin, P. J. King, U. Khan, K. Young, A. Gaucher, S. De, R. J. Smith, I. V. Shvets, S. K. Arora, G. Stanton, H. Y. Kim, K. Lee, G. T. Kim, G. S. Duesberg, T. Hallam, J. J. Boland, J. J. Wang, J. F. Donegan, J. C. Grunlan, G. Moriarty, A. Shmeliov, R. J. Nicholls, J. M. Perkins, E. M. Grieveson, K. Theuwissen, D. W. McComb, P. D. Nellist, V. Nicolosi, *Science* **2011**, *331*, 568.
[3] X. Zhang, Q.-H. Tan, J.-B. Wu, W. Shi, P.-H. Tan, *Nanoscale* **2016**, *8*, 6435.
[4] R. V. Gorbachev, I. Riaz, R. R. Nair, R. Jalil, L. Britnell, B. D. Belle, E. W. Hill, K. S. Novoselov, K. Watanabe, T. Taniguchi, A. K. Geim, P. Blake, *Small* **2011**, *7*, 465.
[5] K. Xu, Z. Wang, F. Wang, Y. Huang, F. Wang, L. Yin, C. Jiang, J. He, *Adv. Mater.* **2015**, *27*, 7881.
[6] D. S. Kong, W. H. Dang, J. J. Cha, H. Li, S. Meister, H. L. Peng, Z. F. Liu, Y. Cui, *Nano Lett.* **2010**, *10*, 2245.
[7] J. Zhang, Z. Peng, A. Soni, Y. Zhao, Y. Xiong, B. Peng, J. Wang, M. S. Dresselhaus, Q. Xiong, *Nano Lett.* **2011**, *11*, 2407.
[8] Q. H. Wang, K. Kalantar-Zadeh, A. Kis, J. N. Coleman, M. S. Strano, *Nat. Nanotechnol.* **2012**, *7*, 699.
[9] M. Chhowalla, H. S. Shin, G. Eda, L. J. Li, K. P. Loh, H. Zhang, *Nat. Chem.* **2013**, *5*, 263.
[10] X. Zhang, X. F. Qiao, W. Shi, J. B. Wu, D. S. Jiang, P. H. Tan, *Chem. Soc. Rev.* **2015**, *44*, 2757.
[11] D. J. Late, B. Liu, H. S. S. R. Matte, C. N. R. Rao, V. P. Dravid, *Adv. Funct. Mater.* **2012**, *22*, 1894.
[12] W. Feng, J.-B. Wu, X. Li, W. Zheng, X. Zhou, K. Xiao, W. Cao, B. Yang, J.-C. Idrobo, L. Basile, W. Tian, P. Tan, P. Hu, *J. Mater. Chem. C* **2015**, *3*, 7022.
[13] K. S. Novoselov, A. K. Geim, S. V. Morozov, D. Jiang, Y. Zhang, S. V. Dubonos, I. V. Grigorieva, A. A. Firsov, *Science* **2004**, *306*, 666.
[14] M. N. Ali, J. Xiong, S. Flynn, J. Tao, Q. D. Gibson, L. M. Schoop, T. Liang, N. Haldolaarachchige, M. Hirschberger, N. P. Ong, R. J. Cava, *Nature* **2014**, *514*, 205.
[15] Q. Song, X. Pan, H. Wang, K. Zhang, Q. Tan, P. Li, Y. Wan, Y. Wang, X. Xu, M. Lin, X. Wan, F. Song, L. Dai, *Sci. Rep.* **2016**, *6*, 29254.
[16] K. S. Novoselov, A. H. Castro Neto, *Phys. Scr.* **2012**, *T146*, 014006.
[17] F. Xia, H. Wang, Y. Jia, *Nat. Commun.* **2014**, *5*, 4458.
[18] L. Li, Y. Yu, G. J. Ye, Q. Ge, X. Ou, H. Wu, D. Feng, X. H. Chen, Y. Zhang, *Nat. Nanotechnol.* **2014**, *9*, 372.
[19] X. F. Qiao, X. L. Li, X. Zhang, W. Shi, J. B. Wu, T. Chen, P. H. Tan, *Appl. Phys. Lett.* **2015**, *106*, 223102.
[20] C. Xia, J. Li, *J. Semicond.* **2016**, *37*, 051001.
[21] Z. Lou, Z. Liang, G. Shen, *J. Semicond.* **2016**, *37*, 091001.
[22] L. Tao, D. Wang, S. Jiang, Y. Liu, Q. Xie, H. Tian, N. Deng, X. Wang, Y. Yang, T. Ren, *J. Semicond.* **2016**, *37*, 041001.
[23] X. S. Li, Y. W. Zhu, W. W. Cai, M. Borysiak, B. Y. Han, D. Chen, R. D. Piner, L. Colombo, R. S. Ruoff, *Nano Lett.* **2009**, *9*, 4359.
[24] Y. Sui, J. Appenzeller, *Nano Lett.* **2009**, *9*, 2973.
[25] Y. M. Lin, C. Dimitrakopoulos, K. A. Jenkins, D. B. Farmer, H. Y. Chiu, A. Grill, P. Avouris, *Science* **2010**, *327*, 662.
[26] B. Radisavljevic, A. Radenovic, J. Brivio, V. Giacometti, A. Kis, *Nat. Nanotechnol.* **2011**, *6*, 147.
[27] Y. W. Zhu, S. Murali, M. D. Stoller, K. J. Ganesh, W. W. Cai, P. J. Ferreira, A. Pirkle, R. M. Wallace, K. A. Cychosz, M. Thommes, D. Su, E. A. Stach, R. S. Ruoff, *Science* **2011**, *332*, 1537.
[28] D. Xiao, G. B. Liu, W. X. Feng, X. D. Xu, W. Yao, *Phys. Rev. Lett.* **2012**, *108*, 196802.
[29] S. Kim, A. Konar, W. S. Hwang, J. H. Lee, J. Lee, J. Yang, C. Jung, H. Kim, J. B. Yoo, J. Y. Choi, Y. W. Jin, S. Y. Lee, D. Jena, W. Choi, K. Kim, *Nat. Commun.* **2012**, *3*, 1011.
[30] F. Xia, H. Wang, D. Xiao, M. Dubey, A. Ramasubramaniam, *Nat. Photonics* **2014**, *8*, 899.
[31] E. F. Liu, Y. J. Fu, Y. J. Wang, Y. Q. Feng, H. M. Liu, X. G. Wan, W. Zhou, B. G. Wang, L. B. Shao, C. H. Ho, Y. S. Huang, Z. Y. Cao, L. G. Wang, A. D. Li, J. W. Zeng, F. Q. Song, X. R. Wang, Y. Shi, H. T. Yuan, H. Y. Hwang, Y. Cui, F. Miao, D. Y. Xing, *Nat. Commun.* **2015**, *6*, 6991.
[32] K. S. Novoselov, A. K. Geim, S. V. Morozov, D. Jiang, M. I. Katsnelson, I. V. Grigorieva, S. V. Dubonos, A. A. Firsov, *Nature* **2005**, *438*, 197.
[33] K. F. Mak, C. Lee, J. Hone, J. Shan, T. F. Heinz, *Phys. Rev. Lett.* **2010**, *105*, 136805.
[34] A. Splendiani, L. Sun, Y. Zhang, T. Li, J. Kim, C.-Y. Chim, G. Galli, F. Wang, *Nano Lett.* **2010**, *10*, 1271.
[35] A. A. Balandin, S. Ghosh, W. Z. Bao, I. Calizo, D. Teweldebrhan, F. Miao, C. N. Lau, *Nano Lett.* **2008**, *8*, 902.
[36] C. Lee, X. D. Wei, J. W. Kysar, J. Hone, *Science* **2008**, *321*, 385.
[37] R. R. Nair, P. Blake, A. N. Grigorenko, K. S. Novoselov, T. J. Booth, T. Stauber, N. M. R. Peres, A. K. Geim, *Science* **2008**, *320*, 1308.
[38] A. K. Geim, K. S. Novoselov, *Nat. Mater.* **2007**, *6*, 183.
[39] M. S. Xu, T. Liang, M. M. Shi, H. Z. Chen, *Chem. Rev.* **2013**, *113*, 3766.
[40] C. H. Lui, Z. Li, Z. Chen, P. V. Klimov, L. E. Brus, T. F. Heinz, *Nano Lett.* **2010**, *11*, 164.
[41] C. Cong, T. Yu, K. Sato, J. Shang, R. Saito, G. F. Dresselhaus, M. S. Dresselhaus, *ACS Nano* **2011**, *5*, 8760.
[42] J. B. Wu, X. Zhang, M. Ijäs, W. P. Han, X. F. Qiao, X. L. Li, D. S. Jiang, A. C. Ferrari, P. H. Tan, *Nat. Commun.* **2014**, *5*, 5309.
[43] J. B. Wu, Z. X. Hu, X. Zhang, W. P. Han, Y. Lu, W. Shi, X. F. Qiao, M. Ijias, S. Milana, W. Ji, A. C. Ferrari, P. H. Tan, *ACS Nano* **2015**, *9*, 7440.
[44] X. Lu, M. Utama, J. Lin, X. Luo, Y. Zhao, J. Zhang, S. T. Pantelides, W. Zhou, S. Y. Quek, Q. Xiong, *Adv. Mater.* **2015**, *27*, 4502.
[45] X. Luo, X. Lu, C. Cong, T. Yu, Q. Xiong, S. Y. Quek, *Sci. Rep.* **2015**, *5*, 14565.
[46] A. A. Puretzky, L. Liang, X. Li, K. Xiao, K. Wang, M. Mahjouri-Samani, L. Basile, J. C. Idrobo, B. G. Sumpter, V. Meunier, D. B. Geohegan, *ACS Nano* **2015**, *9*, 6333.
[47] X. F. Qiao, J. B. Wu, L. W. Zhou, J. S. Qiao, W. Shi, T. Chen, X. Zhang, J. Zhang, W. Ji, P. H. Tan, *Nanoscale* **2016**, *8*, 8324.
[48] A. K. Geim, I. V. Grigorieva, *Nature* **2013**, *499*, 419.
[49] H. Fang, C. Battaglia, C. Carraro, S. Nemsak, B. Ozdol, J. S. Kang, H. A. Bechtel, S. B. Desai, F. Kronast, A. A. Unal, G. Conti, C. Conlon, G. K. Palsson, M. C. Martin, A. M. Minor, C. S. Fadley, E. Yablonovitch, R. Maboudian, A. Javey, *Proc. Natl. Acad. Sci. USA* **2014**, *111*, 6198.
[50] X. Wang, F. Xia, *Nat. Mater.* **2015**, *14*, 264.
[51] F. Withers, O. Del Pozo-Zamudio, A. Mishchenko, A. P. Rooney, A. Gholinia, K. Watanabe, T. Taniguchi, S. J. Haigh, A. K. Geim, A. I. Tartakovskii, K. S. Novoselov, *Nat. Mater.* **2015**, *14*, 301.
[52] B. Partoens, F. M. Peeters, *Phys. Rev. B* **2006**, *74*, 075404.
[53] W. J. Zhao, Z. Ghorannevis, L. Q. Chu, M. L. Toh, C. Kloc, P. H. Tan, G. Eda, *ACS Nano* **2013**, *7*, 791.
[54] Y. L. Li, A. Chernikov, X. Zhang, A. Rigosi, H. M. Hill, A. M. van der Zande, D. A. Chenet, E. M. Shih, J. Hone, T. F. Heinz, *Phys. Rev. B* **2014**, *90*, 205422.
[55] S. Zhang, J. Yang, R. Xu, F. Wang, W. Li, M. Ghufran, Y.-W. Zhang, Z. Yu, G. Zhang, Q. Qin, Y. Lu, *ACS Nano* **2014**, *8*, 9590.
[56] X. Wang, A. M. Jones, K. L. Seyler, V. Tran, Y. Jia, H. Zhao, H. Wang, L. Yang, X. Xu, F. Xia, *Nat. Nanotechnol.* **2015**, *10*, 517.
[57] Q. J. Song, Q. H. Tan, X. Zhang, J. B. Wu, B. W. Sheng, Y. Wan, X. Q. Wang, L. Dai, P. H. Tan, *Phys. Rev. B* **2016**, *93*, 115409.
[58] K. Kim, J.-U. Lee, D. Nam, H. Cheong, *ACS Nano* **2016**, *10*, 8113.
[59] A. Molina-Sanchez, L. Wirtz, *Phys. Rev. B* **2011**, *84*, 155413.
[60] P. Blake, E. W. Hill, A. H. C. Neto, K. S. Novoselov, D. Jiang, R. Yang, T. J. Booth, A. K. Geim, *Appl. Phys. Lett.* **2007**, *91*, 063124.

[61] Z. H. Ni, H. M. Wang, J. Kasim, H. M. Fan, T. Yu, Y. H. Wu, Y. P. Feng, Z. X. Shen, *Nano Lett.* **2007**, *7*, 2758.
[62] I. Jung, M. Pelton, R. Piner, D. A. Dikin, S. Stankovich, S. Watcharotone, M. Hausner, R. S. Ruoff, *Nano Lett.* **2007**, *7*, 3569.
[63] H. Li, J. M. T. Wu, X. Huang, G. Lu, J. Yang, X. Lu, Q. H. Zhang, H. Zhang, *ACS Nano* **2013**, *7*, 10344.
[64] C. Casiraghi, A. Hartschuh, E. Lidorikis, H. Qian, H. Harutyunyan, T. Gokus, K. S. Novoselov, A. C. Ferrari, *Nano Lett.* **2007**, *7*, 2711.
[65] L. Malard, M. Pimenta, G. Dresselhaus, M. Dresselhaus, *Phys. Rep.* **2009**, *473*, 51.
[66] A. C. Ferrari, J. C. Meyer, V. Scardaci, C. Casiraghi, M. Lazzeri, F. Mauri, S. Piscanec, D. Jiang, K. S. Novoselov, S. Roth, A. K. Geim, *Phys. Rev. Lett.* **2006**, *97*, 187401.
[67] P. H. Tan, W. P. Han, W. J. Zhao, Z. H. Wu, K. Chang, H. Wang, Y. F. Wang, N. Bonini, N. Marzari, N. Pugno, G. Savini, A. Lombardo, A. C. Ferrari, *Nat. Mater.* **2012**, *11*, 294.
[68] M. Bruna, S. Borini, *Appl. Phys. Lett.* **2009**, *94*, 031901.
[69] Y. Li, Y. Rao, K. F. Mak, Y. You, S. Wang, C. R. Dean, T. F. Heinz, *Nano Lett.* **2013**, *13*, 3329.
[70] W. Jie, X. Chen, D. Li, L. Xie, Y. Y. Hui, S. P. Lau, X. Cui, J. Hao, *Angew. Chem., Int. Ed.* **2015**, *54*, 1185.
[71] H. Zeng, G.-B. Liu, J. Dai, Y. Yan, B. Zhu, R. He, L. Xie, S. Xu, X. Chen, W. Yao, X. Cui, *Sci. Rep.* **2013**, *3*, 1608.
[72] X. L. Li, X. F. Qiao, W. P. Han, Y. Lu, Q. H. Tan, X. L. Liu, P. H. Tan, *Nanoscale* **2015**, *7*, 8135.
[73] Y. K. Koh, M. H. Bae, D. G. Cahill, E. Pop, *ACS Nano* **2011**, *5*, 269.
[74] V. G. Kravets, A. N. Grigorenko, R. R. Nair, P. Blake, S. Anissimova, K. S. Novoselov, A. K. Geim, *Phys. Rev. B* **2010**, *81*, 155413.
[75] E. D. Palik, *Handbook of Optical Constants of Solids*, Academic Press, New York **1985**.
[76] X. Qin, Y. Chen, Y. Liu, L. Zhu, Y. Li, Q. Wu, W. Huang, *J. Semicond.* **2016**, *37*, 013002.
[77] N. Mao, J. Tang, L. Xie, J. Wu, B. Han, J. Lin, S. Deng, W. Ji, H. Xu, K. Liu, L. Tong, J. Zhang, *J. Am. Chem. Soc.* **2015**, *138*, 300.
[78] J.-B. Wu, H. Zhao, Y. Li, D. Ohlberg, W. Shi, W. Wu, H. Wang, P.-H. Tan, *Adv. Opt. Mater.* **2016**, *4*, 756.
[79] W. P. Han, Y. M. Shi, X. L. Li, S. Q. Luo, Y. Lu, P. H. Tan, *Acta Phys. Sin.* **2013**, *62*, 110702.
[80] Y. Lu, X. L. Li, X. Zhang, J. B. Wu, P. H. Tan, *Sci. Bull.* **2015**, *60*, 806.
[81] D. Cole, J. Shallenberger, S. Novak, R. Moore, M. Edgell, S. Smith, C. Hitzman, J. Kirchhoff, E. Principe, W. Nieveen, F. Huang, S. Biswas, R. Bleiler, K. Jones, *J. Vac. Sci. Technol., B* **2000**, *18*, 440.
[82] J. W. Park, H. S. So, S. Kim, S. H. Choi, H. Lee, J. Lee, C. Lee, Y. Kim, *J. Appl. Phys.* **2014**, *116*, 183509.
[83] J.-B. Wu, H. Wang, X.-L. Li, H. Peng, P.-H. Tan, *Carbon* **2016**, *110*, 225.
[84] A. C. Ferrari, D. M. Basko, *Nat. Nanotechnol.* **2013**, *8*, 235.
[85] X. Zhang, W. P. Han, J. B. Wu, S. Milana, Y. Lu, Q. Q. Li, A. C. Ferrari, P. H. Tan, *Phys. Rev. B* **2013**, *87*, 115413.
[86] X. L. Li, X. F. Qiao, W. P. Han, X. Zhang, Q. H. Tan, T. Chen, P. H. Tan, *Nanotechnology* **2016**, *27*, 145704.
[87] W. J. Zhao, P. H. Tan, J. Zhang, J. Liu, *Phys. Rev. B* **2010**, *82*, 245423.
[88] X. Zhang, W.-P. Han, X.-F. Qiao, Q.-H. Tan, Y.-F. Wang, J. Zhang, P.-H. Tan, *Carbon* **2016**, *99*, 118.
[89] R. S. Sundaram, M. Engel, A. Lombardo, R. Krupke, A. C. Ferrari, P. Avouris, M. Steiner, *Nano Lett.* **2013**, *13*, 1416.
[90] T. Cao, G. Wang, W. P. Han, H. Q. Ye, C. R. Zhu, J. R. Shi, Q. Niu, P. H. Tan, E. Wang, B. L. Liu, J. Feng, *Nat. Commun.* **2012**, *3*, 887.
[91] H. L. Zeng, J. F. Dai, W. Yao, D. Xiao, X. D. Cui, *Nat. Nanotechnol.* **2012**, *7*, 490.
[92] K. F. Mak, K. L. He, J. Shan, T. F. Heinz, *Nat. Nanotechnol.* **2012**, *7*, 494.
[93] G. Froehlicher, E. Lorchat, F. Fernique, C. Joshi, A. Molina-Sánchez, L. Wirtz, S. Berciaud, *Nano Lett.* **2015**, *15*, 6481.
[94] C. Lee, H. Yan, L. E. Brus, T. F. Heinz, J. Hone, S. Ryu, *ACS Nano* **2010**, *4*, 2695.
[95] H. Li, Q. Zhang, C. C. R. Yap, B. K. Tay, T. H. T. Edwin, A. Olivier, D. Baillargeat, *Adv. Funct. Mater.* **2012**, *22*, 1385.
[96] S. L. Li, H. Miyazaki, H. Song, H. Kuramochi, S. Nakaharai, K. Tsukagoshi, *ACS Nano* **2012**, *6*, 7381.
[97] X. Luo, Y. Zhao, J. Zhang, Q. Xiong, S. Y. Quek, *Phys. Rev. B* **2013**, *88*, 075320.
[98] H. Terrones, E. Del Corro, S. Feng, J. M. Poumirol, D. Rhodes, D. Smirnov, N. R. Pradhan, Z. Lin, M. A. T. Nguyen, A. L. Elias, T. E. Mallouk, L. Balicas, M. A. Pimenta, M. Terrones, *Sci. Rep.* **2014**, *4*, 4215.
[99] W. J. Zhao, Z. Ghorannevis, K. K. Amara, J. R. Pang, M. Toh, X. Zhang, C. Kloc, P. H. Tan, G. Eda, *Nanoscale* **2013**, *5*, 9677.
[100] S. Tongay, H. Sahin, C. Ko, A. Luce, W. Fan, K. Liu, J. Zhou, Y. S. Huang, C. H. Ho, J. Y. Yan, D. F. Ogletree, S. Aloni, J. Ji, S. S. Li, J. B. Li, F. M. Peeters, J. Q. Wu, *Nat. Commun.* **2014**, *5*, 3252.
[101] Y. Q. Feng, W. Zhou, Y. J. Wang, J. Zhou, E. F. Liu, Y. J. Fu, Z. H. Ni, X. L. Wu, H. T. Yuan, F. Miao, B. G. Wang, X. G. Wan, D. Y. Xing, *Phys. Rev. B* **2015**, *92*, 054110.
[102] Y. Zhao, X. Luo, J. Zhang, J. Wu, X. Bai, M. Wang, J. Jia, H. Peng, Z. Liu, S. Y. Quek, Q. Xiong, *Phys. Rev. B* **2014**, *90*, 245428.
[103] Y. Zhao, J. Qiao, P. Yu, Z. Hu, Z. Lin, S. P. Lau, Z. Liu, W. Ji, Y. Chai, *Adv. Mater.* **2016**, *28*, 2399.
[104] M. K. Jana, A. Singh, D. J. Late, C. R. Rajamathi, K. Biswas, C. Felser, U. V. Waghmare, C. Rao, *J. Phys.: Condens. Matter* **2015**, *27*, 285401.
[105] Y. Y. Wang, Z. H. Ni, Z. X. Shen, H. M. Wang, Y. H. Wu, *Appl. Phys. Lett.* **2008**, *92*, 043121.
[106] D. Yoon, H. Moon, Y. W. Son, J. S. Choi, B. H. Park, Y. H. Cha, Y. D. Kim, H. Cheong, *Phys. Rev. B* **2009**, *80*, 125422.
[107] H. Zhao, J. B. Wu, H. X. Zhong, Q. S. Guo, X. M. Wang, F. N. Xia, L. Yang, P. H. Tan, H. Wang, *Nano Res.* **2015**, *8*, 3651.
[108] A. Castellanos-Gomez, L. Vicarelli, E. Prada, J. O. Island, K. L. Narasimha-Acharya, S. I. Blanter, D. J. Groenendijk, M. Buscema, G. A. Steele, J. V. Alvarez, H. W. Zandbergen, J. J. Palacios, H. S. J. van der Zant, *2D Mater.* **2014**, *1*, 025001.
[109] W. Zhao, P. H. Tan, J. Liu, A. C. Ferrari, *J. Am.Chem. Soc.* **2011**, *133*, 5941.
[110] W. Shi, M.-L. Lin, Q.-H. Tan, X.-F. Qiao, J. Zhang, P.-H. Tan, *2D Mater.* **2016**, *3*, 025016.
[111] C. H. Lui, Z. Ye, C. Keiser, X. Xiao, R. He, *Nano Lett.* **2014**, *14*, 4615.
[112] Y. Zhao, X. Luo, H. Li, J. Zhang, P. T. Araujo, C. K. Gan, J. Wu, H. Zhang, S. Y. Quek, M. S. Dresselhaus, Q. Xiong, *Nano Lett.* **2013**, *13*, 1007.
[113] X. Ling, L. Liang, S. Huang, A. A. Puretzky, D. B. Geohegan, B. G. Sumpter, J. Kong, V. Meunier, M. S. Dresselhaus, *Nano Lett.* **2015**, *15*, 4080.
[114] X. Luo, X. Lu, G. K. W. Koon, A. H. Castro Neto, B. Ozyilmaz, Q. Xiong, S. Y. Quek, *Nano Lett.* **2015**, *15*, 3931.
[115] S. Bhagavantam, H. M. Otte, *Phys. Today* **2009**, *20*, 75.
[116] T. Wieting, J. Verble, *Phys. Rev. B* **1972**, *5*, 1473.
[117] M.-L. Lin, F.-R. Ran, X.-F. Qiao, J.-B. Wu, W. Shi, Z.-H. Zhang, X.-Z. Xu, K.-H. Liu, H. Li, P.-H. Tan, *Rev. Sci. Instrum.* **2016**, *87*, 053122.
[118] T. Wieting, J. Verble, *Phys. Rev. B* **1971**, *3*, 4286.
[119] X. Li, W. Cai, J. An, S. Kim, J. Nah, D. Yang, R. Piner, A. Velamakanni, I. Jung, E. Tutuc, S. K. Banerjee, L. Colombo, R. S. Ruoff, *Science* **2009**, *324*, 1312.
[120] S. Tongay, J. Suh, C. Ataca, W. Fan, A. Luce, J. S. Kang, J. Liu, C. Ko, R. Raghunathanan, J. Zhou, F. Ogletree, J. Li, J. C. Grossman, J. Wu, *Sci. Rep.* **2013**, *3*, 2657.

[121] H. Nan, Z. Wang, W. Wang, Z. Liang, Y. Lu, Q. Chen, D. He, P. Tan, F. Miao, X. Wang, J. Wang, Z. Ni, *ACS Nano* **2014**, *8*, 5738.
[122] J. Wilson, A. Yoffe, *Adv. Phys.* **1969**, *18*, 193.
[123] A. Beal, J. Knights, W. Liang, *J. Phys. C: Solid State Phys.* **1972**, *5*, 3540.
[124] B. Wu, H. M. Tuncer, M. Naeem, B. Yang, M. T. Cole, W. I. Milne, Y. Hao, *Sci. Rep.* **2014**, *4*, 4130.
[125] W. Choi, M. Y. Cho, A. Konar, J. H. Lee, G.-B. Cha, S. C. Hong, S. Kim, J. Kim, D. Jena, J. Joo, S. Kim, *Adv. Mater.* **2012**, *24*, 5832.
[126] A. Castellanos-Gomez, J. Quereda, H. P. van der Meulen, N. Agraït, G. Rubio-Bollinger, *Nanotechnology* **2016**, *27*, 115705.
[127] E. Hecht, *Optics*, Addison Wesley Longman, Reading, MA **1998**, 77.
[128] T. Low, A. Rodin, A. Carvalho, Y. Jiang, H. Wang, F. Xia, A. C. Neto, *Phys. Rev. B* **2014**, *90*, 075434.
[129] O. B. Aslan, D. A. Chenet, A. M. van der Zande, J. C. Hone, T. F. Heinz, *ACS Photonics* **2015**, *3*, 96.
[130] S. Lei, L. Ge, S. Najmaei, A. George, R. Kappera, J. Lou, M. Chhowalla, H. Yamaguchi, G. Gupta, R. Vajtai, A. D. Mohite, P. M. Ajayan, *ACS Nano* **2014**, *8*, 1263.
[131] K. Albe, A. Klein, *Phys. Rev. B* **2002**, *66*, 073413.
[132] T. Cheiwchanchamnangij, W. R. Lambrecht, *Phys. Rev. B* **2012**, *85*, 205302.
[133] H.-P. Komsa, A. V. Krasheninnikov, *Phys. Rev. B* **2012**, *86*, 241201.
[134] A. Ramasubramaniam, *Phys. Rev. B* **2012**, *86*, 115409.
[135] D. Y. Qiu, F. H. da Jornada, S. G. Louie, *Phys. Rev. Lett.* **2013**, *111*, 216805.
[136] Z. Ye, T. Cao, K. O'Brien, H. Zhu, X. Yin, Y. Wang, S. G. Louie, X. Zhang, *Nature* **2014**, *513*, 214.
[137] K. He, N. Kumar, L. Zhao, Z. Wang, K. F. Mak, H. Zhao, J. Shan, *Phys. Rev. Lett.* **2014**, *113*, 026803.
[138] B. Zhu, X. Chen, X. Cui, *Sci. Rep.* **2015**, *5*, 9218.
[139] Y.-R. Shen, *Principles of Nonlinear Optics*, Wiley-Interscience, New York **1984**.
[140] P. Hu, Z. Wen, L. Wang, P. Tan, K. Xiao, *ACS Nano* **2012**, *6*, 5988.
[141] L. Plucinski, R. Johnson, B. Kowalski, K. Kopalko, B. Orlowski, Z. Kovalyuk, G. Lashkarev, *Phys. Rev. B* **2003**, *68*, 125304.
[142] L. M. Malard, T. V. Alencar, A. P. M. Barboza, K. F. Mak, A. M. de Paula, *Phys. Rev. B* **2013**, *87*, 201401.
[143] W.-T. Hsu, Z.-A. Zhao, L.-J. Li, C.-H. Chen, M.-H. Chiu, P.-S. Chang, Y.-C. Chou, W.-H. Chang, *ACS Nano* **2014**, *8*, 2951.
[144] M. L. Trolle, Y.-C. Tsao, K. Pedersen, T. G. Pedersen, *Phys. Rev. B* **2015**, *92*, 161409.
[145] X. Zhou, J. Cheng, Y. Zhou, T. Cao, H. Hong, Z. Liao, S. Wu, H. Peng, K. Liu, D. Yu, *J. Am. Chem. Soc.* **2015**, *137*, 7994.